Elevated HLA-E and NKG2A as a consequence of chronic immune activation defines resistance to *M. bovis* BCG immunotherapy in Non-Muscle-Invasive Bladder Cancer

D. Ranti[1,2*], Y.A. Wang[1,2*], J. Daza[1,2*], C. Beiber[1,2], B. Salomé[1], E. Merritt[3], J.A. Cavallo[1], E. Hegewisch-Solloa[4], E.M. Mace[4], A.M. Farkas[5], S. Shroff[3,6], M. Tran[5], J. Qi[7], M. Patel[7], D. Geanon[7], G. Kelly[7], R.M.de Real[7], B. Lee[7], S. Kim-Schulze[7], T.H. Thin[8], M. Garcia-Barros[8], K.G. Beaumont[3,6], Y-C. Wang[3,6], L. Wang[3,9], D. LaRoche[10], Y. lee[10], R.P. Sebra[3,6,9,11], R. Brody[8], A. Tocheva[3], B. Hopkins[1], P. Wiklund[2], J. Zhu[3,9], M.D. Galsky[5], N. Bhardwaj[5], J.P. Sfakianos[2#], A. Horowitz[1#]

[1]Department of Oncological Sciences, Precision Immunology Institute, Tisch Cancer Institute, Icahn School of Medicine at Mount Sinai, New York, NY
[2]Department of Urology, Icahn School of Medicine at Mount Sinai, New York, NY
[3]Department of Genetics and Genomic Sciences, Icahn School of Medicine at Mount Sinai, New York, New York.
[4]Department of Pediatrics, Vagelos College of Physicians and Surgeons, Columbia University, New York NY USA 10032
[5]Division of Hematology and Medical Oncology, Tisch Cancer Institute, Precision Immunology Institute, Icahn School of Medicine at Mount Sinai, New York, NY
[6]Icahn Institute for Data Science and Genomics Technology, Icahn School of Medicine at Mount Sinai, New York, New York
[7]Human Immune Monitoring Center, Icahn School of Medicine at Mount Sinai, New York, New York, USA.
[8]Pathology, Molecular and Cell-Based Medicine, Icahn School of Medicine at Mount Sinai, New York, New York, USA.
[9]Sema4, a Mount Sinai venture, Stamford, Connecticut.
[10]HTG Molecular Diagnostics, Tucson, Arizona
[11]Black Family Stem Cell Institute, Icahn School of Medicine at Mount Sinai, New York, New York.
* These authors contributed equally
# Co-Senior author

Running title. HLA-E and NKG2A in BCG Resistance

Keywords. Bladder cancer; non-muscle invasive bladder cancer; BCG resistance; NK cell; immunotherapy;

Financial support, including the source and number of grants, for each author

Corresponding Author:
Amir Horowitz, PhD
Assistant Professor of Oncological Sciences
Icahn Medical Institute
1425 Madison Ave., Box 1630
New York, New York 10029
Tel: (212) 659-9391 | Fax: (646) 537-9577
Email: amir.horowitz@mssm.edu

Conflict of Interest Disclosure Statement: The authors declare no potential conflicts of interest.
Word Count: 7,000
Fig. Count: 6

Abstract: *Mycobacterium bovis* Bacillus Calmette-Guerin (BCG), the first line treatment for non-muscle invasive bladder cancer (NMIBC), promotes production of type I interferons, particularly interferon (IFN)-γ. Prolonged inflammation and IFN-γ exposure are known to cause an adaptive immune response, enabling immune escape and proliferation by tumor cells. We investigated HLA-E and NKG2A, a novel T and NK cell checkpoint pathway, as a driver of adaptive resistance in BCG unresponsive NMIBC. We observed ubiquitous inflammation in all patients after BCG immunotherapy, regardless of recurrence status. IFN-γ was shown to drive tumor expression of HLA-E and PD-L1. Further, NKG2A-expressing NK and CD8 T cells were enriched in BCG unresponsive tumors and with enhanced capacity for cytolytic functions. Strikingly, *in situ* spatial analyses revealed that HLA-E^{BRIGHT} tumors are activated to recruit NK and T cells via chemokine production potentially sparing HLA-$E^{DIM/NEG}$ tumors that would otherwise be susceptible to lysis. Finally, blood-derived NK cells retained antitumor functions at time of tumor recurrence. These data support combined NKG2A and PD-L1 blockade for BCG unresponsive disease.

Introduction

The only FDA-approved, first-line treatment for high-risk non-muscle-invasive bladder cancer (NMIBC) is intravesical *Mycobacterium bovis* Bacillus Calmette-Guerin (BCG), which is hypothesized to act in part via the release of type I cytokines, notably IFN-γ (1). Tumor recurrence following BCG immunotherapy is common, with local recurrence rates between 32.6 to 42.1% and progression rates between 9.5 to 13.4% (2). Radical cystectomy is the only definitive treatment option for BCG-unresponsive patients, leaving patients at high risk for possible complications and diminished quality of life (3,4). Currently, there is substantial interest and numerous ongoing clinical trials to identify novel therapeutic options for patients with BCG-unresponsive NMIBC.

Despite BCG's use as a first-line immunotherapy to treat NMIBC for over 30 years, the mechanisms underlying the ability of tumor cells to elude the therapeutic benefits of BCG are poorly understood. BCG's six-dose induction regimen was devised anecdotally based on the packaging of BCG used in the seminal study by Morales et al. (5). Only a single dosing study has been performed to assess the immunologic response with this dosing regimen, which concluded that six doses stimulated an immune response but did not investigate the ramifications of the magnitude nor the duration of that immune response (6). Contributing to the difficulty in predicting BCG response is the variety of immune cell lineages implicated in its success, including neutrophils, monocytes, macrophages, dendritic cells (DCs), T cells, and natural killer (NK) cells (7).

Adaptive immune resistance, in which cancers are recognized by the immune cells, but adaptive changes prevent effective immune clearance, is an important mechanism of therapeutic resistance (8). IFN-γ, a prominently BCG-induced cytokine, has been shown to have both pro- and anti-tumorigenic functions across an array of different tumor indications (9). The equilibrium established by IFN-γ signaling may be critical in preventing therapeutic resistance. In melanoma and lung cancer, dysfunctional and overactive IFN-γ pathway signaling is known to drive T cell exhaustion via upregulation of PD-L1 (10). In settings of chronic infection and inflammation, a host-target stalemate can occur due to persistently elevated interferon signaling, the blockage of which can help reduce viral burden (11-13). The impact of long-term intravesical BCG administration, which leads to immune stimulation via IFN-γ secretion, and its role in immune dysregulation and immune cell exhaustion in BCG unresponsive NMIBC is currently unknown.

Previous work comparing BCG-unresponsive tumors to pre-treatment samples showed a significant increase in PD-L1 expression on the unresponsive samples (14). Immunotherapeutic strategies, especially those interrupting the PD-1/PD-L1 axis, designed to unleash exhausted immune cells have improved NMIBC treatment. This led to the use of PD-1 inhibitors to be studied and eventually approved for BCG

unresponsive *carcinoma in situ*. Unfortunately, response rates remain low, at ~19% durable response at 12 months (15-18). Furthermore, PD-L1 expression levels have failed to accurately predict response to immunotherapy in NMIBC, suggesting that alternative mechanisms of immune suppression are important (19).

Recently, the HLA-E and NKG2A axis has been identified as a potent immune checkpoint regulating both CD8 T and NK cells (20-22). Abrogation of NKG2A on NK cells increased effector activity against tumor cells and potentiated anti-tumor function (20,22); and blocking NKG2A on CD8 T cells in a murine model potentiated tumor vaccine response, even in a PD-1 resistant setting (20,22). In this study, we posed a novel hypothesis that BCG induces changes in the bladder tumor microenvironment (TME) including expression of NKG2A and PD-1 on CD8 T cells, NKG2A on NK cells and HLA-E and PD-L1 on tumor cells and these phenotypic changes are mechanistically linked to treatment resistance and tumor recurrence. Important to BCG immunotherapy, HLA-E has been shown to increase in the setting of IFN-γ release (23). This study investigates HLA-E and NKG2A as a novel axis of resistance induced by chronic inflammation and demonstrates a potential combination strategy in NKG2A and PD-L1 blockade for overcoming resistance to BCG immunotherapy for treating NMIBC.

Results

Clinical cohort description.

Patient characteristics of the longitudinal cohort are shown in *Table 1*. For our in situ *mRNA* analysis, 36 samples from 27 unique patients were collected. For our multiplexed urinalysis, 42 samples collected over the course of 26 patients' treatment were used. For single-cell RNA sequencing (scRNAseq), six samples from 5 patients were used. For 10x spatial transcriptomics sequencing (ST-seq) analyses, 20 sequenced slices from 9 unique patients were used. Lastly, for CyTOF, 16 samples from 16 unique patients at the BCG-unresponsive stage were used.

IFN-γ Mediates Adaptive Resistance in BCG-unresponsive Tumors.

To investigate a potential mechanism of adaptive resistance in NMIBC, we used tumor specimens from BCG-unresponsive and BCG naïve tumors collected from a longitudinal cohort of NMIBC patients. Targeted *in situ mRNA* sequencing was performed, and a gene-set enrichment analysis (GSEA) comparing BCG-unresponsive tumors to pre-treatment timepoints (**Fig. 1A***)* (24). Statistically significant gene sets are shown ranked by their normalized enrichment score (NES) (**Fig. 1A**, Supplemental Table S1*)*. The top enriched gene-set comparing BCG-unresponsive tumors includes IFN-γ signature, B cell markers,

cytotoxic lymphocytes, lymphocyte receptors/function, T cell checkpoint modulation, tumor inflammation, TH1 response, lymphocyte trafficking, general T cell markers, and receptor genes. Gene sets that are downregulated in the BCG-unresponsive state and upregulated in the BCG naïve state are TGF beta signaling, hypoxia, peroxisome, oxidative phosphorylation, P53 pathway, DNA repair, and stress toxicity.

Differences in individual genes between paired BCG naive and BCG-unresponsive samples reveal that all paired samples show upregulation of CCL4 and CCL5 and near-universal downregulation of PPP1R15A and IKBKB (**Fig. 1B**; all $p < 0.05$). CCL4 and CCL5 are potent chemo attractants for a variety of cells, among which are NK and T cells (25,26). IKBKB is an activator of NF-κB-dependent apoptotic pathways and PPP1R15A, whose functions associate with negative regulation of TGF-β signaling (27,28).

Validating our *mRNA* analysis at the protein-level, we used the OLINK™ "inflammation panel", a 92-analyte protein proximity extension assay, to profile urine cytokines reflective of the urothelial microenvironment (29,30), from our longitudinal BCG-treated cohort of NMBIC patients. Upregulated cytokines in the sixth dose compared with the BCG naïve state include IFN-γ, Flt3L, IL2RB, CCL19, CCL23, CXCL1, CXCL9, CXCL10, CXCL11, MCP.2, MCP.4 and TWEAK (**Fig. 1C**; all $p<0.05$).

To better understand the effects of IFN-γ on tumor dysregulation, we incubated primary tumor cells from NMIBC patients (n=10) and commercial urothelial cell lines in the presence of recombinant human IFN-γ (**Fig. 1D** and **E**) and measured HLA-E and PD-L1 via fluorescence flow cytometry after 24-hours. In **Fig. 1D**, a histogram (left) and bar plot show sorted CD45- cells from primary NMIBC tumors before and after IFN-γ stimulation. The CD45- cells show statistically significant increases in PD-L1 and HLA-E following stimulation with IFN-γ. Expanding the analysis to commercial immortalized cell lines (n=11) shows the signature is consistent: PD-L1 and HLA-E experience statistically significantly increase after a 24-hour incubation with IFN-γ. Furthermore, we saw no effects on HLA-E expression in WT K562 cells or HLA-E–transfected K562 cells, in which HLA-E expression is controlled under a very strong CMV promoter.

NK and CD8 T cell-derived IFN-γ drives HLA-E expression on BCG-unresponsive tumors through dysregulated STAT1.

Single-cell RNA sequencing (scRNA-seq) on five NMIBC samples was performed to further refine the associated IFN-γ genes. Similarly, we analyzed a cohort of BCG naive and unresponsive tumors. (**Supplementary Table S1**). 24,166 cells containing 26,520 gene features passed quality control and were used for subsequent analyses, with a median of 958 genes detected per cell. (Supplementary Fig. S1).

Twenty-eight identifiable cell populations, including CD8 T cells, regulatory T cells (Tregs), non-CD8 (*CD4*$^-$ *CD8A*$^-$ *FOXP3*$^-$) T cells, NK cells, dendritic cells (DCs), monocytes and macrophages,

granulocytes, B cells, plasma cells, and nonhematopoietic fibroblasts, epithelium, and tumor cells were identified after graph-based clustering (**Fig. 2A**, **Supplementary Table S2**). To identify the cell origins of IFN-γ and related pro-inflammatory gene signatures, we examined the expression of *IFNG* in each of the cell populations. We found that *IFNG* expression was almost exclusively found in tissue-resident memory (TRM) CD8 T cells, canonical CD8 T cells, NK cells, and in CD8- T cells, and with 55.16%, 37.78%, 25.02%, and 14.00% of cells with *IFNG* > 0, respectively.

As NK and non-regulatory T cells demonstrated the highest level of *IFNG* expression among all cell populations, we investigated the effects of NK and T cell-derived IFN-γ signaling on tumor cells. To do so, we employed NicheNet, an algorithm that uses a combination of transcriptomic data, known ligand-receptor interactions, and gene-gene signaling and regulatory relationships to predict potential interactions between cells of interest (31). The top five predicted ligands for inducing tumor expression of IFN-γ response genes were interferon-gamma (*IFNG*), tumor necrosis factor (*TNF*), CD45 (*PTPRC*), transforming growth factor (TGF)-beta (*TGFB1*), and high mobility group box 1 (*HMGB1*) (**Fig. 2B**). TRM CD8 T cells expressed the highest levels of *IFNG* and *HMGB1* relative to NK and CD8 T cells, while *TNF* and *TGFB1* expressions were highest in non-TRM CD8 T cells and NK cells, respectively (**Fig. 2B**). Putative receptors of these ligands, including *IFNGR1*, *IFNGR2*, *TNFRSF1A*, and *LTBR*, were most highly expressed in the BCG-unresponsive samples, suggesting the presence of corresponding signaling activity in the tumor (**Fig. 2B**). To further examine genes upregulated in the tumor as a consequence of signals from NK and T cells, we created a circos plot demonstrating predicted relationships between 'sender' or effector ligands and 'receiver' genes (**Fig. 2C**). Aside from CD45, all other top-ranked ligands were predicted to induce expression of IFN-γ response genes to varying degrees. The strongest predicted target of *IFNG* and *TNF* was intercellular adhesion molecule 1 (*ICAM1*), a cell surface glycoprotein commonly found expressed on endothelial cells and immune cells with roles in cell migration. Additionally, genes involved in apoptosis, TNF-related ligands and receptors, inflammatory response, and interferon-gamma signaling were also predicted to be upregulated as a result of sender ligand signaling by tumor cells (**Fig. 2C**).

A downstream target of IFN-γ signaling, *HLA-E* is predicted to be under direct regulation of transcriptional regulators *STAT1*, *MYC*, and *NFKB1*, with *STAT1* predicted to have the strongest regulatory potential for *HLA-E* expression (**Fig. 2D**, **Supplementary Table S3**). Among these, *STAT1* is also a target gene that is upregulated in bladder tumor cells as a result of IFN-γ signaling from NK and CD8 T/TRM cells (**Fig. 2C**). We further confirmed the *STAT1-HLA-E* axis in the in situ targeted *mRNA* analysis of NMIBC patients, which demonstrated a direct positive correlation (Spearman rho = 0.455, p-value = 2.74e-3) between *STAT1* and *HLA-E* expression (**Fig. 2E**). Though *MYC*, *NFKB1*, and *IFNG* were also predicted to exert some degree of regulatory effect on *HLA-E* expression, these genes failed to show a direct correlation with *HLA-E* expression by targeted *mRNA* analysis (**Supplementary Fig. S2**).

CD8 T cells preferentially infiltrate activated tumor "nano-environments" with higher densities of HLA-E that actively recruit CD8 T cells via production of CXCL9/10/11.

To spatially resolve the relationship between tumor nests and immune infiltrates, we performed a series of 10X ST-seq analyses. 20 total slices of tumor were sequenced from four treatment-naïve and four BCG-unresponsive tumors including one unresponsive tumor treated with BCG and PD-1 blockade (**Fig. 3**). Spatial relationships were investigated on the 'nano-environment' level, defined as a Visium dot with a radius of 2.5 adjacent Visium spots, or roughly ~138 microns. A representative tumor section is shown to highlight a neighbors analysis showing the intensity of neighboring T cell infiltration, and a topographical map of HLA-E expressing cell density is overlaid on top (**Fig. 3A**). In order to investigate the effects of IFN-ɣ, the same representative tumor slice was colored with scored *IFNGR1*/2 expression (**Fig. 3B**). Strikingly we found greatest expression of *IFNGR1*/*R2* in areas of dense HLA-E expressing cells. An alternative view of binarized HLA-E density with NK and CD8 T cells are shown in magenta and red, respectively (**Fig. 3C**). High HLA-E-expressing (HLA-E^{BRIGHT}) Visium spots are shown in blue, and no/low HLA-E Visium spots shown in tan. We observed very clear clustering of CD8 T cells around HLA-E^{BRIGHT} spots and high-HLA-E density areas. Conversely, we only observed very sparse NK or T cells overall in the treatment-naïve tumor sections (data not shown). To better understand the mechanisms underlying the preferential infiltration of HLA-E^{BRIGHT} tumor nests, we profiled expression of chemokines. Strikingly, we observed that HLA-E^{BRIGHT} tumors were significantly more enriched for elevated expression of *CXCL9*, *CXCL10*, and *CXCL11* (**Fig. 3D**). Collectively, the data demonstrate that HLA-E^{BRIGHT} tumors are activated to recruit T cells. Importantly, this observation was unique to HLA-E^{BRIGHT} tumors and not seen at all in the treatment-naïve specimens (data not shown). These data are supported by two previous studies of melanoma showing that IFNs (type I or II) induce CXCL9/10/11 by tumors and attract $CXCR3^{+}$ T cells to the TME.(32,33)

Expanding to a meta-analysis of the entire cohort of tumor sections, a differential gene expression analysis was performed on Visium spots identified as encompassing tumor cells stratified by the number of neighboring infiltrating T cells (**Fig. 3E-3G**). Indeed, we observed significantly greater numbers of CD8 T cells surrounding HLA-E^{BRIGHT} tumor spots (**Fig. 3E**). We next profiled expression of key inhibitory ligands expressed on tumors *CD47*, *CD274* (PD-L1), *PDCD2*, and *CD58,* along with *HLA-A*, *-B*, *-C*, *-E*, and *IFNGR1*/*R2* (**Fig. 3F**). Expression levels all were increased on tumor spots

as the numbers of infiltrating CD8 T cells increased. The *class I HLA* genes were most sensitive to increasing T cell infiltration, followed by *CD58* and *CD274* (PD-L1). Additionally, interferon pathway genes were also enriched in the tumor nests that are more intensely infiltrated by T cells: *JAK1*, *JAK2*, *STAT1*, *IRF1*, *IRF9*, and *FAS* were all significantly upregulated. Importantly, *SOCS1* and *STAT3* were not upregulated with increasing tumor infiltration. Whereas STAT3 signals are critical for production of IL-6 and IL-10, Suppressor of Cytokine Signaling Protein-1 (SOCS1) plays a critical role in negative feedback inhibition to shut down inflammatory immune responses through targeting JAK1 and JAK2 for proteosomal degradation.(34-36) Finally, the spatial neighbors' analysis was expanded to investigate Visium spots containing tumors stratified by HLA-E and infiltrating T cells, with high infiltration being > 7 neighboring T cells and low infiltration being < 4 neighboring T cells. The HLA-$E^{DIM/NEG}$ condition had only 90 tumor Visium spots, or 6.5%, classified as being highly by infiltrated T cells; the HLA-E^{BRIGHT} condition had 410, or 29.8%, of tumor Visium spots classified as being highly infiltrated by T cells. Further, the HLA-E^{BRIGHT} tumor Visium spots showed the same upregulation as when classified by highly infiltrated by tumor cells, and were enriched in *CD47*, *CD274* (PD-L1), *PDCD2*, *HLA-A*, *-B*, *-C*, *-E*, *CD58, IFNGR1, IFNGR2, JAK1, JAK2, STAT1, IRF1, IRF9,* and FAS.

***KLRC1* (NKG2A) expression stratifies NK and CD8 T cell capacity for anti-tumor functions in BCG-unresponsive tumors.**

Given the hypothesis that NKG2A presents a novel immune checkpoint receptor in bladder cancer, we sought to characterize the cytolytic capacity of immune populations most impacted by NKG2A expression. Stratifying by KLRC1 expression on immune populations defines distinct phenotypes of cytolytic activity. (**Fig. 4A**). Our data has identified that *KLRC1*$^{+}$ CD8 T cells expressed elevated *GNLY*, *TIGIT*, *GZMA*, *GZMB*, *HAVCR2*, *LAG3*, and *CTLA4*. CD8 TRM cells showed significant upregulation in *GNLY*, *GZMA*, *GZMB*, *LAG3*, *TIGIT*, and *HAVCR2* in the *KLRC1*$^{+}$ cells. Finally, a similar analysis of NK cells showed significant upregulation in *XCL1*, *TIGIT*, *XCL2*, and *GZMK* between *KLRC1*$^{+}$ cells.

To better understand if elevated expression of cytolytic genes in NKG2A^{+} NK, CD8 T, and TRM cell populations correlated with improved functional sensitivity, we used mass cytometry (CyTOF) to profile the *in vitro* response to BCG by blood-derived NK cells from NMIBC patients at time of tumor recurrence. We performed a phenograph clustering analysis(37) to stratify the data by their likelihood of existing in the ex-vivo state vs. the experimental state, using either an assay of antibody-dependent cellular cytotoxicity (ADCC) reactivity or loss of class I HLA 'missing-self' stimulation conditions. Highly polarized clusters of immune cells underwent a differential protein expression analysis, MELD, comparing levels of important markers that dominantly defined the ex-vivo vs. highly experimental conditions (38).

Blood-derived NK cells at the time of recurrence experience retained anti-tumor abilities when stimulated by ADCC-inducing or missing-self conditions (**Fig. 4B** and **C**). Clusters highly likely to be found in the ADCC-induced condition after 6 hours of stimulation express statistically significantly higher levels CD107a, MIP1β, XCL1, TNFα, IFN-γ, and NKG2A. The ADCC-induced condition expressed statistically significantly lower granzymes a, b, k, and perforin, DNAM1, NKp46, and CD16 suggesting tumor lysis as well as maturation during the time of co-culture. Additionally, are activating receptors, which are known to be down-regulated during maturation (DNAM-1, NKp46) or following CD16-ligation to IgG-TIGIT, an inhibitory checkpoint receptor that competes with DNAM-1 for ligand, was also downregulated as was the terminal maturation marker, CD57, suggesting the dominantly activated NK cells were maturing but not exhausted. Similarly, NK cells highly polarized towards the missing-self condition after 6 hours of stimulation and showed statistically significant increases in expression of CD107a, MIP1β, XCL1, TNFα, IFN-γ, and NKG2A; and statistically significant decreases in granzymes a, b and k; perforin; DNAM1; NKp46; TIGIT; CD57; and CD16.

Discussion:

Adaptive immune resistance can be driven be either/both tumor-intrinsic and extrinsic mechanisms for overcoming cytolytic immune clearance(39,40). Evidence from both mouse and human studies demonstrates that interferons, while stimulating a robust anti-tumor response, also upregulate immune-suppressive factors in the setting of prolonged exposure. In melanoma, IFN-γ from CD8 T cells were shown to upregulate PD-L1 and $FOXP3^{+}$ regulatory pathways (41). In a broader pan-cancer (n=18) study that included bladder cancer, high cytokine conditions were associated with counter-inflammatory pathways, including PD-L1/2 (42,43). Despite the potential for inducing immune exhaustion, IFN-γ is well known to provide beneficial anti-tumor inflammation and is a critical pathway for successful anti-PD-L1 therapy (44). Anti-tumor inflammation, therefore, exists along a continuum where an equilibrium is necessary for appropriate immunotherapeutic efficacy (**Fig. 5**) (45).

Using both prospective and retrospective cohorts of NMIBC patients who underwent BCG immunotherapy, we investigated the impact of prolonged BCG-induced inflammation on the interplay between tumor and immune cell populations. Our data suggests: i) inflammation was ubiquitous in BCG-responders and non-responders alike; ii) IFN-γ directly contributes to the upregulation of HLA-E and PD-L1 on NMIBC tumors; iii) NKG2A levels stratify NK and T cells by both cytolytic ability and expression of secondary inhibitory checkpoint receptors; iv) Unique to BCG-unresponsive tumors, HLA-E^{BRIGHT} tumor nests were activated to produce CXCL9/10/11 and strongly correlated with infiltration by CD8 T cells; v) tumors stratified by neighboring infiltrated immune cells reveal a program of activation (and possibly

dysregulation) alongside adaptive upregulation of immunosuppressive ligands for NK and T cells; and vi.) NK cells removed from their suppressive microenvironment demonstrated retained functional capacity. These findings support a picture of immune dysregulation, defined partly by increased HLA-E and PD-L1, in the setting of BCG-induced chronic activation and inflammation.

Intravesical administration of BCG is initiated as an adjuvant immunotherapy, as complete tumor resection is the initial diagnostic and therapeutic step, which, given the context, presupposes inflammation without active tumor to clear (46). Dosing and immune profiling studies on the immune system throughout the course of BCG administration have never been performed, and thus insights into the immune status on the continuum between inactive to dysregulated are unavailable (**Fig. 5**).

Our findings suggest that all NMIBC patients at the time of tumor recurrence show signs of a hallmark immune response to BCG, led by IFN-γ. BCG-unresponsive tumors see uniform increases in chemotactic cytokines and inflammatory pathways that should otherwise function to suppress their growth. Furthermore, checkpoint levels profiled on BCG-unresponsive tumors saw increases in their expression, suggesting that inflammatory stimuli have been prolonged and allowed for triggering feedback mechanisms responsible for immune evasion. Therefore, when tumors recur, for reasons beyond the scope of this study, they are met by a functional status of the immune system ill-equipped to suppress it.

Novel to our study is our analysis of spatially resolved insights into the potential consequences of IFN-γ dysregulation on immune migration patterns. Preferential infiltration of high-HLA-E and high-PD-L1 tumor nests by immune cells was seen in with areas of high CXCL9, 10, and 11. The phenomenon of tumors producing CXCL9/10/11 has been shown previously in melanoma, where IFN-γ was shown to induce CXCL9/10/11 production, increasing the chemotactic gradient for $CXCR3^+$ T cells (33,47). The tumor nests producing high CXCL9/10/11 show upregulated mediators of cytokine production, including *IRF1*, *IRF9*, and *JAK2*, as well as absent expression of cytokine-suppressing mediators, like *SOCS1*. These tumor nests are notably upregulated for immunosuppressing ligands as well: highly infiltrated T cell tumor areas are HLA-E, CD47, PD-L1, and PDCD2-bright areas. Combined, these data suggest that the HLA-E and PD-L1 bright tumor nests may be luring cells towards the tumor nano-environments best equipped to suppress their cytolytic activities.

This study has notable limitations. Our sample sizes, while being the largest NMIBC spatial sequencing cohort available, are small and present a potentially limited view of the disease. Furthermore, both spatial sequencing and single-cell RNA sequencing have known difficulties detecting transcripts from several genes, several of which were pertinent to our study: among others, CD4, GAS2, GAS3, FASL, IFN-γ, and CXCR3 were poorly expressed in our spatial dataset.

Together, our analyses suggest that the current guidelines on checkpoint inhibition in NMIBC could be improved via a multi-cell-targeting immunotherapy approach. Randomized trials from multiple bladder

and adjacent tumor type trials have shown that PD-1/PD-L1 stratification fails to predict response to immunotherapy with PD-1/PD-L1 antibodies: IMvigor210, JAVELIN bladder 100, and CheckMate-275 (NCT02108652, NCT01772004, NCT02387996) all saw that PD-1/PD-L1 biomarker stratification did not effectively stratify response rates. Combined NK and T cell strategies are actively being explored in existing clinical trials, such as the COAST trial (NCT03822351) in stage III unresectable non-small cell lung cancer. COAST compares durvalumab (anti-PD-L1) to combination with monalizumab (anti-NKG2A), and interim results show that combination therapy provides substantial gains: combination therapy achieved a 10-month progression-free survival rate of 72.7%, compared to only 39.2% in the durvalumab-only arm (48). Our data support the combination immunotherapeutic approach, indicating that BCG-induced adaptive immune resistance raises PD-L1 levels alongside HLA-E on tumor cells. While this analysis does not exclude the presence of alternative checkpoints, such as TIGIT, TIM3, or LAG3, it lends evidence to the hypothesis that combination NK and T cell immunotherapeutic approaches may hold the key to improved study outcomes for NMIBC.

Conclusions, future work

Our data suggests that inflammation was ubiquitous in all patients after BCG immunotherapy, regardless of their recurrence status, and that IFN-γ directly contributed to the upregulation of HLA-E and PD-L1 in the TME. Furthermore, we found that NKG2A levels partition NK, T, and CD8 T cells by cytolytic ability, with NKG2A$^+$ immune cells expressing increased cytolytic markers alongside checkpoint levels. Lastly, we found that NK cells removed from their suppressive microenvironment demonstrated retained functional capacity in response to missing-self and ADCC reactivity. Future experiments will focus on functional studies, investigating co-culture of paired tumor organoids alongside tumor-infiltrating lymphocytes in the presence and absence of anti-PD-L1 and anti-NKG2A antibodies, as well as validating our evidence in external cohorts of NMIBC patients.

Methods

Patients and samples

Patients at Mount Sinai Hospital (MSH) were enrolled in the study following Institutional Review Board (IRB) approval (protocol 10-1180). 10-1180 covers the use of patient tissues in a biorepository and allows for prospective collection of blood, urine, and tissue samples from enrolled patients. Formalin-fixed paraffin-embedded (FFPE) blocks from patients receiving BCG treatment were obtained retrospectively from the biorepository and prospectively for patients receiving ongoing treatment. For patients followed prospectively, samples were collected on the day of surgery and throughout BCG immunotherapy. Due to IRB limits on the amount of blood collected, blood and urine samples were taken at the first dose, third dose, and sixth dose of the induction cycle; at every follow-up cystoscopy; and at the third maintenance cycle dose. Tumor samples were taken at every possible timepoint. In our study, we defined BCG naïve as any patient who had yet to receive BCG, regardless of past treatment with other chemotherapies. We defined BCG-unresponsive as any patient who received at least 5 / 6 induction doses of BCG and who had a recurrent tumor within 24 doses of induction initiation.

Sample processing

Blood and urine samples from bladder cancer patients were processed to collect PBMCs, serum, and cell-free urine. Blood was spun down (4C, 2000rpm, 10 min) to isolate serum, and PBMCs were collected using Ficoll-Paque isolation. PBMCs were frozen down in a Mr. Frosty at -80 C for 24 hours and stored at -160 C in 10% DMSO and 90% fetal bovine serum; PBMCs and cell-free urine were stored at -80 C.

Tumor tissues obtained from transurethral resections of bladder tumor (TURBT) were placed into RPMI medium immediately after removal and transferred to the laboratory for additional processing. Bladder and lymph nodes obtained from radical cystectomies were sent from the operating room directly to the pathology suite after completion of the lymph node dissection. The bladder was bivalved; samples of visible tumor were extracted and placed in RPMI medium, and the tumor was transferred to the laboratory for additional processing.

Fresh tumor samples underwent a variety of different processing techniques based on the planned experiment. Tumor used for spatial sequencing was placed in a 10 mm x 10 mm cryomold with optimal cutting temperature (OCT) media and frozen down on a thermal block immersed in liquid nitrogen. Tumor tissues were digested using tumor dissociation enzymes (Miltenyi, 130-095-929) and a GentleMACS machine (program 37C_h_TDK_3) at 37C. Mechanically and enzymatically separated tissues were filtered through a 70μM cell strainer and assessed on Countess II (ThermoFisher) for viability and cell numbers.

Targeted RNA sequencing

FFPE sections from 38 retrospective NMIBC cases were obtained from the institutional biorepository and used for targeted RNA sequencing. RNA was extracted from five and ten μm sections. HTG EdgeSeq lysis buffer was added to lyse and permeabilize the samples. Nuclease protection probes (NPPs) were added to the lysed samples and hybridized to the target mRNA. A nuclease was added to digest non-hybridized mRNA and excess NPPs. The nuclease digestion reaction was finalized with a termination solution followed by heat-mediated denaturation of the enzyme.

Each sample was used as a template for PCR reactions with specially designed primers. Each primer contains a unique barcode that is used for sample identification and multiplexing. Samples were analyzed simultaneously on an Illumina sequencing platform to prepare the library. All samples and controls were quantified in triplicates. No template control (NTC) reactions were made for each master mix used during the qPCR process to test the absence of a probe or qPCR contamination. Molecular-grade water was used in place of a test sample in the NTC reactions using the same volume as the template.

Sufficient concentration of sample for library pooling, appropriate dilution for the library pool, and volume of denaturation reagents to add to the library were determined by HTG library calculator. 2N NaOH and heat (98C, 4 minutes) were used for library denaturation. The denatured library was loaded into the well of the NextSeq sequencing cartridge. Sequencing was performed using an Illumina NextSeq sequencer.

The sequencing data on mRNA expression of target genes were imported into HTG EdgeSeq parser software. HTG biostatistics department performed quality control analyses and normalized the data. Data were returned from the sequencer as demultiplexed FASTQ files with four files per assay well. The HTG EdgeSeq parser software aligned the FASTQ files to the probe list and collated the data.

Protein concentration measurement

Cell-free urine supernatant and serum samples were randomized in a 96-well plate. Diluted samples and positive and negative controls were incubated overnight with an incubation mix (incubation solution, incubation stabilizer, A-probes, and B-probes) at 4°C. Samples were then incubated with an extension mix (High purity water, PEA solution, PEA enzyme, PCR polymerase) for 5 min and placed on a thermal cycler. Following the thermal cycler, samples were incubated with a detection mix (detection solution, High purity water, detection enzyme, PCR polymerase) and transferred to a chip. Primers were loaded onto the chip, and the chip was profiled using the Fluidigm IFC controller HX with the Fluidigm Biomark Reader. Data were normalized using extension and interplate controls and a correction factor. The resulting data were reported in normalized protein expression (NPX) units on a log2 scale.

IFN-γ co-culture

Cell lines and CD45- isolated primary tumor cells were incubated in media optimized for high viability for 72 hours (RPMI-1640 supplemented with 20% fetal bovine serum). Tumor cells were expanded until they were confluent in 2 T175 flasks. Following expansion, cells were culture in 100 ng / mL of IFN-γ for a total of 24 hours in a 24 well plate. Following co-culture, cell lines were trypsinized (immortalized), and primary tumors were gently removed from the solid phase by a cell scraper. Samples with and without IFN-γ stimulation were measured for HLA-E and PD-L1 protein expression levels.

HLA-E and PD-L1 levels were assessed via FlowCytometry. Cells were stained in 4C FACS buffer (phosphate-buffered saline (PBS) with 2% heat-inactivated FBS and EDTA 2 mM) for 30 minutes. Subsequently, cells were washed in PBS, incubated for 20 minutes in a viability dye, washed again with PBS, and resuspended in 2% paraformaldehyde. The experiment was performed in triplicate, with three readouts per cell line per experimental condition. FlowCytometry acquisition was performed using an LRS-Fortessa (BD Biosciences), and data were analyzed using the CytoBank software. When staining for HLA-E, cells were first stained 20 minutes with HLA-E prior to staining with additional PD-L1. In CytoBank, several gates were applied to generate the final dataset. A live/dead gate was applied, followed by a gate to remove doublets and isolate singlets. Lastly, the data was arcsinh transformed prior to analysis.

Once the final dataset had been generated, statistical significance between unstimulated and stimulated cell lines was assessed. An independent t-test was run with a significance cutoff of $p < 0.05$.

Targeted RNA sequencing analyses

Prior to any analyses, clinical data on all patients was gathered. The following items were collected for all samples processed by HTG Molecular: patient date of birth; gender; age at BCG induction; BCG status (unresponsive vs. naïve vs. exposed); date of sample collection; stage at collection; grade at collection; recurrence date; time to recurrence; time to progression; BCG start date; BCG last exposure; BCG induction cycle last dose; prior chemotherapy; cystectomy; date of cystectomy; stage at cystectomy.

Following clinical data collection, a gene set enrichment analysis (GSEA) was performed on the targeted RNA sequencing data. Specifically, we used paired patient samples before and after BCG exposure in the BCG recurrent patient population only. We used custom gene sets, as well as all Hallmark gene sets from the Broad Institute's MSigDB, as inputs for the enrichment analysis (24). Statistical significance was set at $p < 0.05$, and gene sets found to be significant are listed in *Supplementary Table 1*. All gene sets found to be statistically significant were evaluated forleading-edgee genes, defined as the genes that contribute most to the enrichment score and associated p-value.

The leading-edge genes from statistically significant gene sets in the GSEA were collated and used to assess for group differences between the paired HTG patient samples. We performed these analyses specifically on the BCG-recurrent cohort. Prior to any analyses, a Shapiro-Wilk's test, chosen for suitability in small sample sizes, was used to assess for normality.(49) All samples with a $p < 0.05$ were considered not normally distributed, and a Kruskal-Wallis test was performed to assess for group differences.(50) All other samples were assessed using an independent T-test. Genes with statistically significant differences between the BCG naïve and the BCG-unresponsive populations were then visualized on radar plots.

Plasma and cell-free urine supernatant protein concentration analysis

We used the OLINK Proteomics®- inflammation panel to validate the signature seen in the Targeted Bulk RNA sequencing data. Protein levels were visualized at BCG naïve, third dose, sixth dose, and first-cystoscopy timepoint, comparing NPX values for all patients between the BCG naïve timepoint and the sixth dose timepoint. In order to determine the suitable statistical test, a Shapiro-Wilk's test was used to assess for normality, and a Kruskal-Wallis test was used in every instance in which one or both samples were not normally distributed. An independent T-test was used in the event both samples were normally distributed. All statistically significant genes between the BCG naïve and sixth induction dose timepoint are shown.

Single cell RNA sequencing:

Data preprocessing

Single cell RNA sequencing (scRNA-seq) analysis was performed using Seurat v4.0.1 in RStudio v1.1.456 with R v4.0.3 (51). Genes expressed in fewer than 3 cells were excluded from later analyses. Cells with < 200 or > 2500 unique genes, as well as cells containing >15% mitochondrial gene transcripts were discarded. Subsequent data normalization was preformed using the NormalizeData function, and consisted of dividing feature counts for each cell by total counts for that cell, scaling by a factor of 10,000, and natural log transformation. 2,000 variable genes in each sample were identified using the FindVariableFeatures function. We then integrated 24,166 cells containing 26,520 genes from five bladder tumor samples via the IntegrateData function, and performed scaling and principal component analysis (PCA) on the integrated data structure using the functions ScaleData and RunPCA, respectively. Using the first 50 principal components (PCs), graph-based clustering was performed using Seurat FindNeighbors and FindClusters functions (resolution = 0.9), and UMAP dimensionality reduction was performed to reveal 28 cell clusters. Cluster-specific marker genes were identified using the FindAllMarkers function, and marker genes with a natural-log fold change (FC) > 0.25 and expressed in >= 25% of cells were used to annotate cell cluster identities based on known cell type markers (52-54): CD8 T cells (*CD8A*, *CD3E*), CD8- T cells (*CD3E*),

tumors (*MUC1*, *KRT7/8/13/17/18*), B cells (*MS4A1*, *CD79A*), monocytes/macrophages (*CD14*, *LYZ*, *FCGR3A*, *MS4A7*), T regulatory cells (*CD3E*, *FOXP3*), granulocytes (*C1QA/B/C*, *ITGAM*, *FCGR3A*), NK (*NKG7*, *GNLY*, *KLRD1*, *KLRF1*), fibroblasts (*COL1A1*, *SPARC*), epithelium (*EMP1*), DC (*FCER1A*, *CST3*, *ITGAX*), plasma cells (*MZB1*, *JCHAIN*, *IGHG3*), and CD8 TRM cells (*CD3E*, *CD8A*, *KLRD1*). Clusters 22, 24, 25, and 26 containing 224, 142, 141, and 101 cells, respectively, were ultimately excluded from further analyses due to unclear cell identities.

NicheNet Analysis

We used the NicheNet R package to infer potential ligand-receptor interactions between NK and T cells and tumor cells as well as potential regulatory effects in tumor gene expression as a result of these interactions (31). We added known ligand-receptor interactions between ligands IgG1 and IgG3 and the receptor CD16 (weight = 1) to NicheNet's default ligand-receptor interactions database, and also integrated the Harmonizome Pathway Commons Protein-Protein Interactions database: (https://maayanlab.cloud/Harmonizome/dataset/Pathway+Commons+Protein-Protein+Interactions) with NicheNet's default signaling network (weight = 1) (55,56). We used the modified ligand-receptor interaction and signaling networks for subsequent analyses. We defined the NK and T cell populations as senders and tumor cells as receivers, and derived a list of 92 receptors expressed in the receiver population by intersecting the list of receptors from the ligand-receptor interaction network with genes expressed in at least 10% of tumor cells in the RNA assay. 50 potential ligands expressed in greater than 10% of the sender NK and T cells were then derived based on their interaction with the list of 92 receptors. We then calculated activity scores for each ligand based on its potential to affect expression of Hallmark interferon gamma response genes (24,57). Statistical analyses including Wilcoxon rank sum tests and Pearson and Spearman correlations were performed using R v4.0.3.

Differential gene expression analysis

Differentially expressed genes (DEGs) between KLRC1+ versus KLRC1- cells were found using the FindMarkers function from the Seurat R package, where cells with KLRC1 expression greater than 0 in the RNA assay were labeled as KLRC1+.

10X Visium spatial sequencing

Tumor samples collected both prospectively and retrospectively were used to generate a potential cohort for spatial sequencing. A 10 μm slice of tumor was hemotoxin and eosin stained (H&E), and reviewed with a board-certified pathologist to verify tissue integrity, the presence of tumor nests, and

immune infiltrates. Three to five 10 μm slices from each tumor were then used for RNA extraction and quantification. A Qiagen RNEasy Mini kit was used for RNA extraction; a ThermoFisher NanoDrop was used to assess extracted RNA concentration; and an Agilent TapeStation was used to identify RNA integrity via the RNA integrity number equivalent (RINe) score. A RINe cutoff of > seven was used as a threshold for good quality.

Of an initial cohort of 55 samples, eight were identified as having good-quality tissue integrity, presence of tumor / immune populations, and high RNA quality. One representative sample from the cohort was used for tissue optimization, which generates the optimal experimental parameters for the spatial sequencing cohort. Tissue optimization consists of 1) tissue permeabilization, 2) fluorescent cDNA synthesis, 3) tissue removal, and 4) slide imaging. Tissue slices are cut onto the capture areas which contain poly(dT) primers for the capture and production of cDNA. After the addition of the master mix containing fluorescently labelled nucleotides, fluorescent cDNA is attached, and can be visualized following enzymatic removal of the tissue. After 7 variable timepoints from 5 minutes to 60 minutes, the optimal duration of permeabilization is determined by the timepoint with the highest fluorescence signal and the lowest signal diffusion.

Using the parameters generated by the tissue optimization step, a cohort of 8 samples was used for the full experimental protocol. Tissues were stained and imaged; cDNA was synthesized; a second cDNA strand was synthesized and denatured; cDNA was generated and the first quality control was performed. Finally, the Visium Spatial gene expression library was constructed, and the second QC was performed. Following library construction, the samples were sequenced and aligned using Illumina platform.

Spatial neighbors, differential gene expression analyses

Spatial sequencing analyses were performed in Python 3.8.8 using Scanpy, Squidpy, AnnData, and the Tangram packages. Data storage and computational job submission were run on Mount Sinai's high-performance computing cluster, Minerva. Each spatial object was normalized, log transformed, and filtered. Visium dots with fewer than 1,000 and more than 35,000 transcribed genes were filtered out. Next, the resulting spatial objects were concatenated into a single object, and genes were filtered out if they appeared in less than 1% of the total number of Visium spots. Labelled scRNA-seq data was then used to project cell-type annotations onto the spatial data in a multi-label multi-class classification algorithm (Tangram). Tangram assigns probabilities that a specific cell type resides in a given Visium spot. Visium spots have a diameter of 55 μm, and therefore multiple cells can reside in a single spot, or "nano-environment." A spot was designated as having a given cell type if the mapped single-cell probability in that spot was > 50%. Lastly, clinical annotations associated with the samples were added to the spatial data to create a complete cohort.

Spatial relationships between tumor cells, immune infiltrates, and relevant genes were then compared visually and numerically. HLA-E expression was binarized for all Visium dots into those expressing any level of HLA-E and those expressing no HLA-E. These binarized data were used to create topographical density plots of HLA-E expression (Fig. 3). HLA-E quartiles were computed, and high HLA-E expressing cells were designated as those > 75th percentile of expression. Lastly, *IFNGR1* and *IFNGR2*, and *CXCL9 - 11* gene scores were created by scoring expression against 150 randomly selected genes to create a single numerical score.

A spatial neighbors' analysis was computed using a radius of 2 Visium dots. Each Visium dot was therefore defined as a function of its surrounding labelled Visium dots, out to 2 rings adjacent. Visium dots containing tumor cells were isolated, and each tumor-containing dot was characterized as a function of its surrounding tumor-infiltrating T cells. A differential gene expression was run, comparing gene expression of the Visium dots with no surrounding infiltrating tumor cells to cohorts of 1 and greater surrounding T cells. An independent T test was used, and the Bonferroni correction was applied to generated adjusted P values.

Mass cytometry antibody preparation and staining

PBMCs from BCG-treated bladder cancer patients at the time of tumor recurrence were isolated using Ficoll-Paque and resuspended in cell medium (RPMI-1640 medium supplemented with 10% heat-inactivated FBS, 1% Penicillin, 1% Streptomycin and 1% L-glutamine). PBMCs were conjugated to antibodies purchased from Fluidigm using the Maxpar X8 and MCP9 labelling kits. Platinum barcodes were prepared as previously described. All antibodies were titrated prior to conjugation.

Prior to mass cytometry staining, all cells were incubated for 20 minutes at 37C in RPMI cell medium (described above) and IdU (Fluidigm, t#201127), Rh103 (Fluidigm, #201103A) and anti-IgG4 if cells were to be co-cultured with K562 and rituximab. Following the incubation, cells were centrifuged, washed with PBS and 0.2% bovine serum albumin (BSA), and incubated for 3 minutes on ice with an Fc-blocking reagent. Samples were washed again with PBS and 0.2% BSA; barcoded samples were pooled together and washed; finally, samples were stained with extracellular antibodies for 30 minutes on ice and in PBS and 0.2% BSA.

When staining four samples, cells were single-barcoded using 194Pt, 195Pt, 196Pt or 198Pt. When staining five or six samples, cells were stained with combination of barcodes. Cells were again washed using PBS 0.2% BSA; barcoded samples were pooled together; samples were washed again, and stained with extracellular antibodies for 30 minutes on ice in PBS 0.2% BSA. Cells were co-cultured in the presence of either K562 and rituximab, Raji cells, or nothing (Med condition), for a total of 6 hours.

Samples were washed with PBS 0.2% BSA and resuspended in Fixation/Perm buffer (Invitrogen, #00-5523-00) for 30 minutes on ice. Cells were centrifuged and washed with Maxpar Barcode Perm Buffer (Fluidigm, #201057) and barcoded using the Cell-ID 20-Plex Pd Barcoding kit (Fluidigm, #201060). Barcoded samples were washed with permeabilization buffer (Invitrogen, #00-5523-00) and pooled. Intracellular staining was then performed in permeabilization buffer with Heparin at a concentration of 100U/mL for 30 minutes on ice. Stained cells were washed with permeabilization buffer and resuspended in PBS with PFA 2.4%, saponin 0.08%, Osmium tetroxide 0.075nM and Ir 0.125uM (Fluidigm, #201192A). Finally, samples were washed and resuspended in PBS 0.2% BSA and data were acquired within four days, or frozen in FBS/DMSO 90/10. The antibody panel in supplemental Table S2 was used to stain bladder cancer patient samples.

Mass cytometry sample acquisition and processing:

Prior to acquisition, samples were washed with cell staining buffer and acquisition solution (Fluidigm). Following washing, samples were resuspended in acquisition solution (1 million cells / 1 mL) containing a 1:20 dilution of EQ normalization beads. Data were then acquired using the Fluidigm Helios mass cytometer with a wide bore injector configuration at an acquisition speed of < 400 cells per second. The output files were normalized and concatenated using Fluidigm's CyTOF software, and outputted as FCS files.

The Mount Sinai Human Immune Monitoring Core's (HIMC) pipeline for processing and cleaning was used to clean the resulting FCS files. Aberrant acquisition time-windows and low DNA intensity events were stripped out by the sample preprocessing pipeline. Samples were then demultiplexed via the cosine similarity of the Palladium barcoding channel on a cell-by-cell basis to every possible barcode used in a batch. Once the cell-barcode labelling has been established, the signal-to-noise (SNR) ratio was calculated by taking the difference between the highest and second highest similarity scores. Cells with low SNR ratios were flagged as multiplets and removed. Finally, acquisition multiplets are removed based on the Gaussian parameters residual and offset acquired by the Helios mass cytometer.

Data processing and analysis:

Data were uploaded onto Cytobank and processed for downstream analyses. Several gates were applied: a live dead gate and a doublets gate in sequential order. All data were arcsinh transformed, and no batch corrections were performed given all samples were run in a single batch. Files were downloaded onto Minerva, concatenated into a single object, and clinical data were assigned to each sample. A phenograph analysis was performed to cluster the cellular data. A MELD analysis was run stratifying samples at the

tumor recurrent timepoint between the ex-vivo state and the K562 or Raji cell states. Highly polarized clusters (<25% average predicted likelihood of being in the ex-vivo state; > 75% average predicted likelihood of being in the Raji or K562 state) were isolated, and a differential protein expression was run.

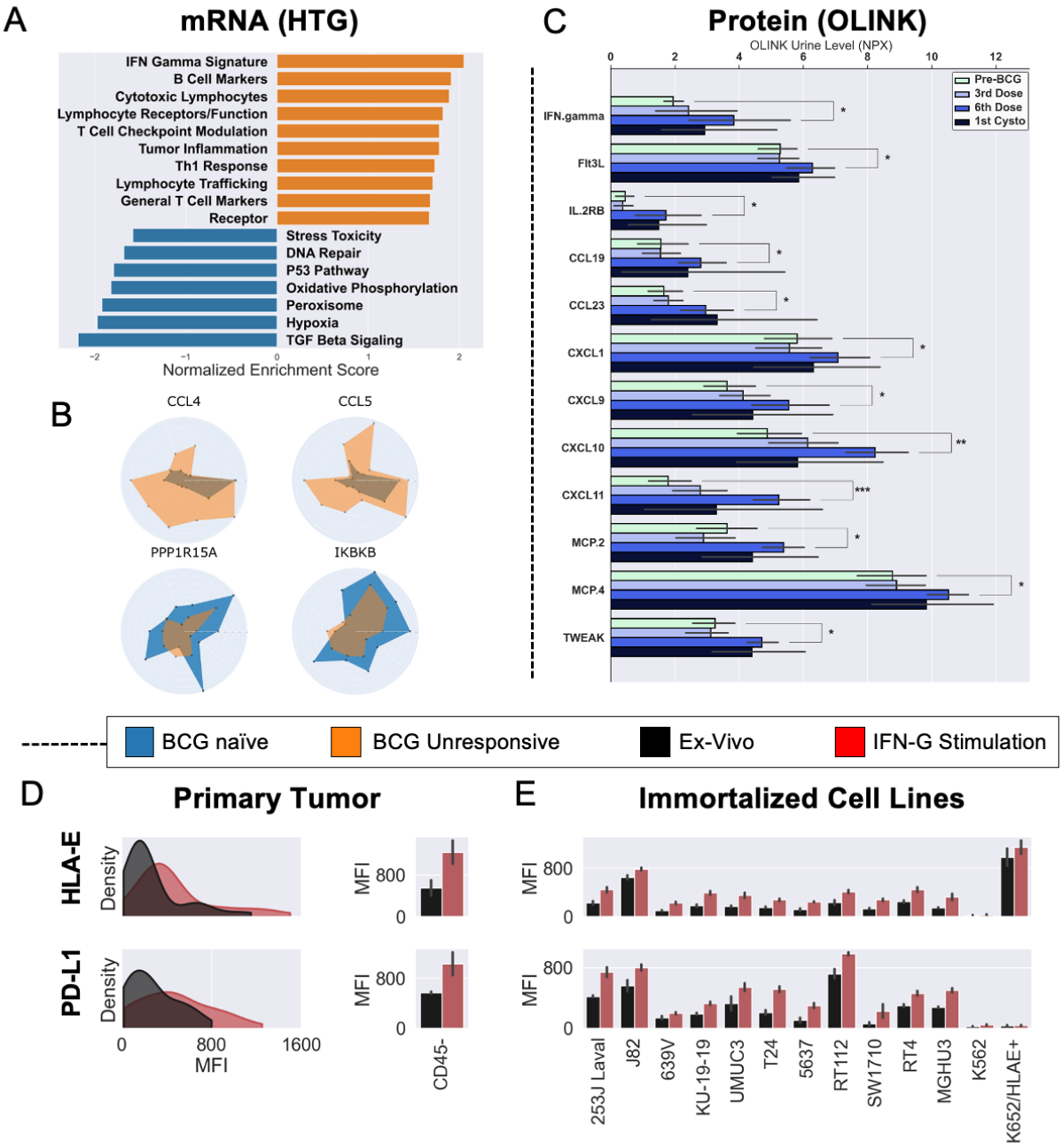

Figure 1: Adaptive resistance in BCG unresponsive disease revealed by bulk RNA sequencing and OLINK proteomics. **A:** Bulk RNA gene-set enrichment analysis showing statistically significant differences between BCG naïve and BCG unresponsive cases. IFN-γ signature is the most highly upregulated signature in the BCG unresponsive patients. All gene sets are significant at $p < 0.05$ by Kruskal-Wallis or independent T-test. **B:** Radar plots, one patient per spoke, showing upregulated individual genes (CCL4 and CCL5), and downregulated individual genes (PPP1R15A and IKBKB). All genes significant at $p < 0.05$. **C:** Longitudinal protein analysis in all patients with comparisons between BCG naïve and 6th induction dose timepoints (* $p < 0.05$, ** $p < 0.001$, *** $p < 0.0001$). **D:** MFI of primary non-muscle invasive bladder cancer cells after 24 hours of incubation with IFN-γ. **E:** MFI of commercial immortalized cell lines after 24 hours of IFN-γ stimulation (all values $p < 0.05$).

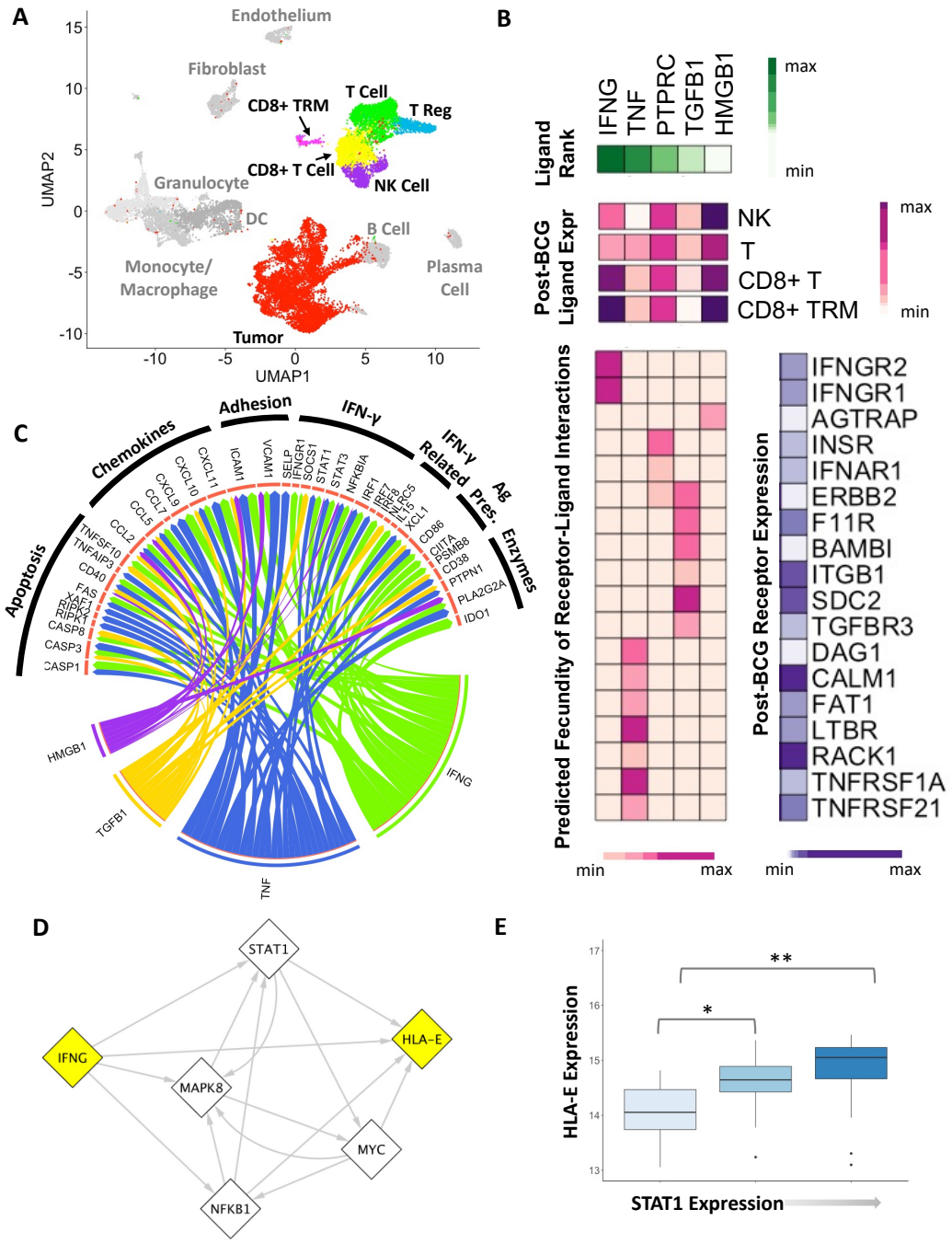

Figure 2: IFN-γ signaling is predicted to drive downstream HLA-E expression via STAT1 in tumor cells. **A:** UMAP visualization of cell types from scRNA-Seq analysis of urothelial tumor samples. **B:** NicheNet predictions of upstream ligand-receptor interactions showing IFNG, TNF, PTPRC, TGFB1, and HMGB1 (left) as the top 5 ligands expressed in NK, T, CD8+ T, and CD8+ TRM cells (middle) that most likely influence tumor cell expression of interferon-gamma signaling genes. Strength of ligand-receptor interactions (top right) and expression of the receptors in tumor cells (bottom right) are also shown. **C:** Circos plot showing links between NicheNet-predicted ligands and downstream interferon-gamma pathway genes. Strong relationships between ligand-target gene pairs are demonstrated by both wider arrow width and solid arrow colors. **D:** NichetNet-predicted regulatory network between IFN-γ and HLA-E. **E:** Expression of HLA-E in HTG targeted RNA-Seq urothelial cancer cohort with respect to STAT1 levels. (*p = 0.0274; **p = 0.00674)

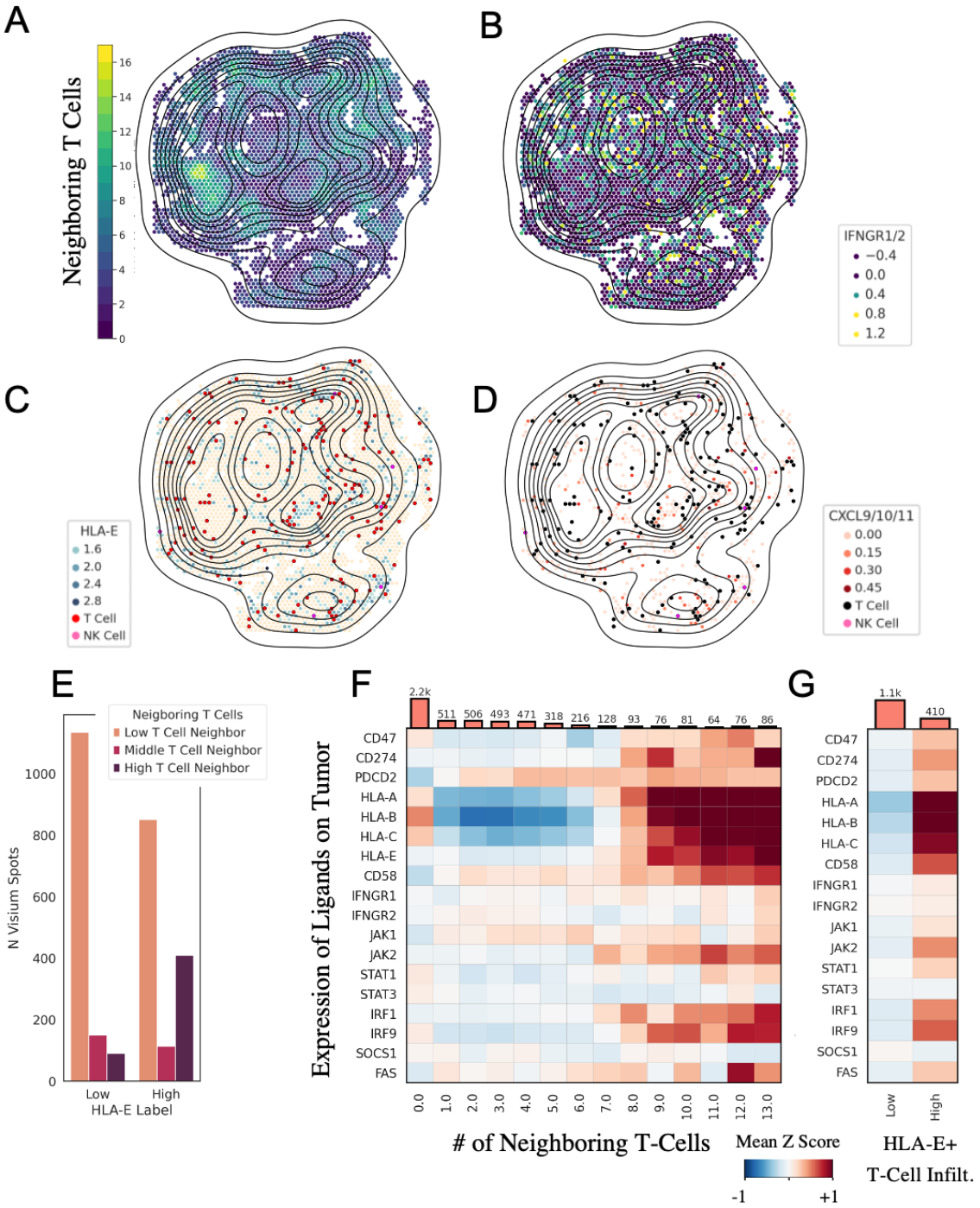

Figure 3: Preferential tumor "nano-environment" infiltration of T cells occurs in tumor nests with higher densities of HLA-E. **A:** representative spatial slice colored by number of neighboring infiltrating T cells, with a topographical plot showing density of HLA-E expression. **B:** representative spatial slice colored by *IFNGR1* and *IFNGR2* score with a topographical plot overlaid showing density of HLA-E expression. **C:** representative spatial slice colored by low HLA-E expressing cells (tan), high HLA-E expressing cells (blue) and immune cells (red and magenta), with a topographical plot overlaid showing density of HLA-E expression. **D:** representative spatial slice showing CXCL9/10/11 score, T cells, NK cells, and an overlaid topographical plot of HLA-E density. **E:** Barplot showing counts of low and high HLA-E tumor cells by surrounding T cell classification (low, medium, and high infiltration).
F: heatmap of all spatial points, BCG naïve and unresponsive, showing pertinent genes z-scored and stratified by number of neighboring infiltrating T-cells. **G:** heatmap of low-HLA-E and low-T cell infiltrated tumor cells vs high-HLA-E and high-T cell infiltrated tumors.

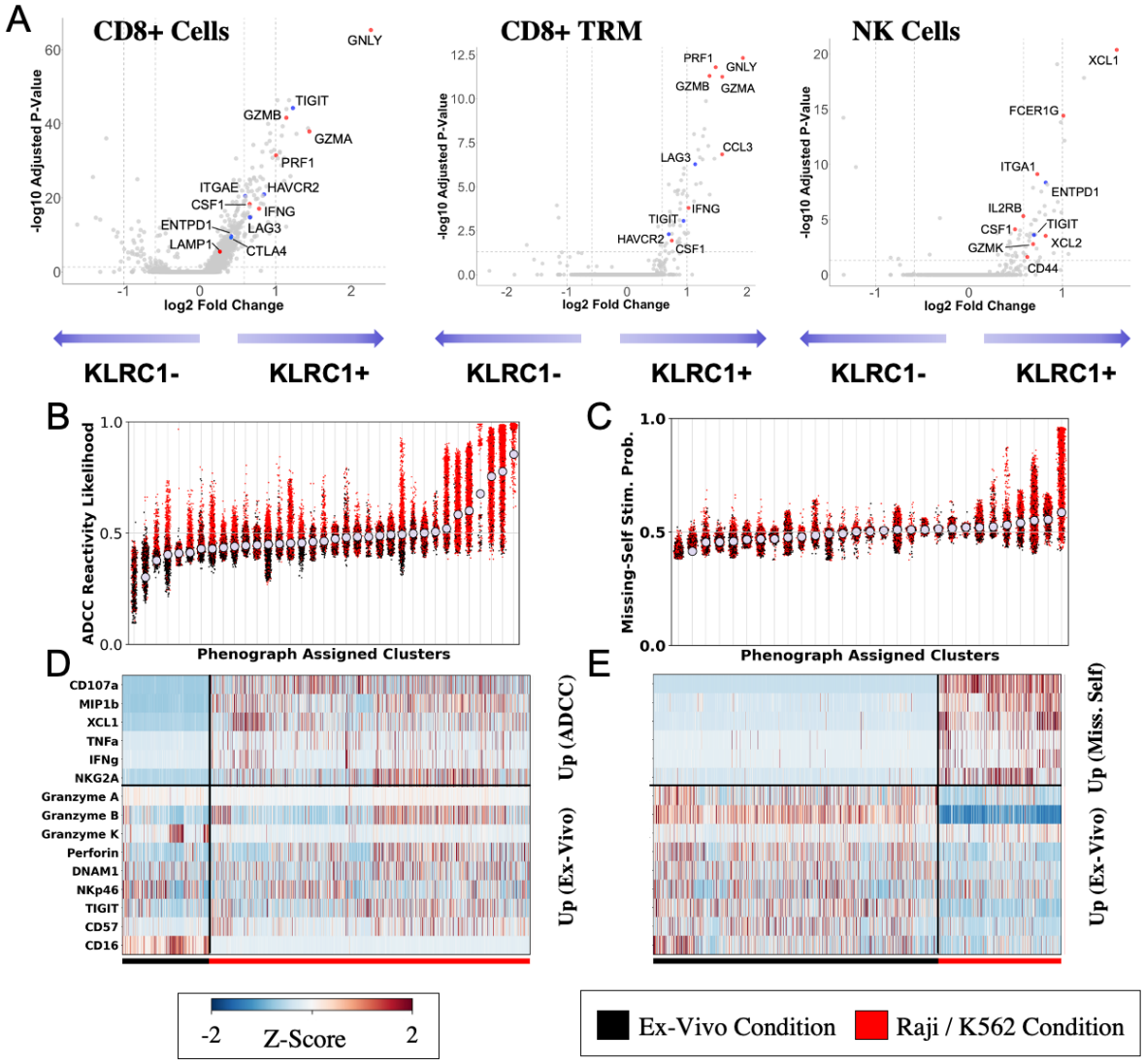

Figure 4: *KLRC1* (NKG2A) expression stratifies NK and CD8+ T cell capacity for anti-tumor functions in BCG unresponsive tumors. A: single-cell RNA sequencing showing statistically significant upregulation of both immune checkpoints and cytotoxic genes in KLRC1+ CD8+ T cells, CD8+ TRMs, and NK cells. B: phenograph clusters stratified by ADCC reactivity. C: phenograph clusters stratified by missing-self reactivity. D: CYTOF markers partitioned by strongly ex-vivo vs strongly ADCC reactive clusters. E: CYTOF markers partitioned by strongly ex-vivo and strongly missing-self reactive clusters.

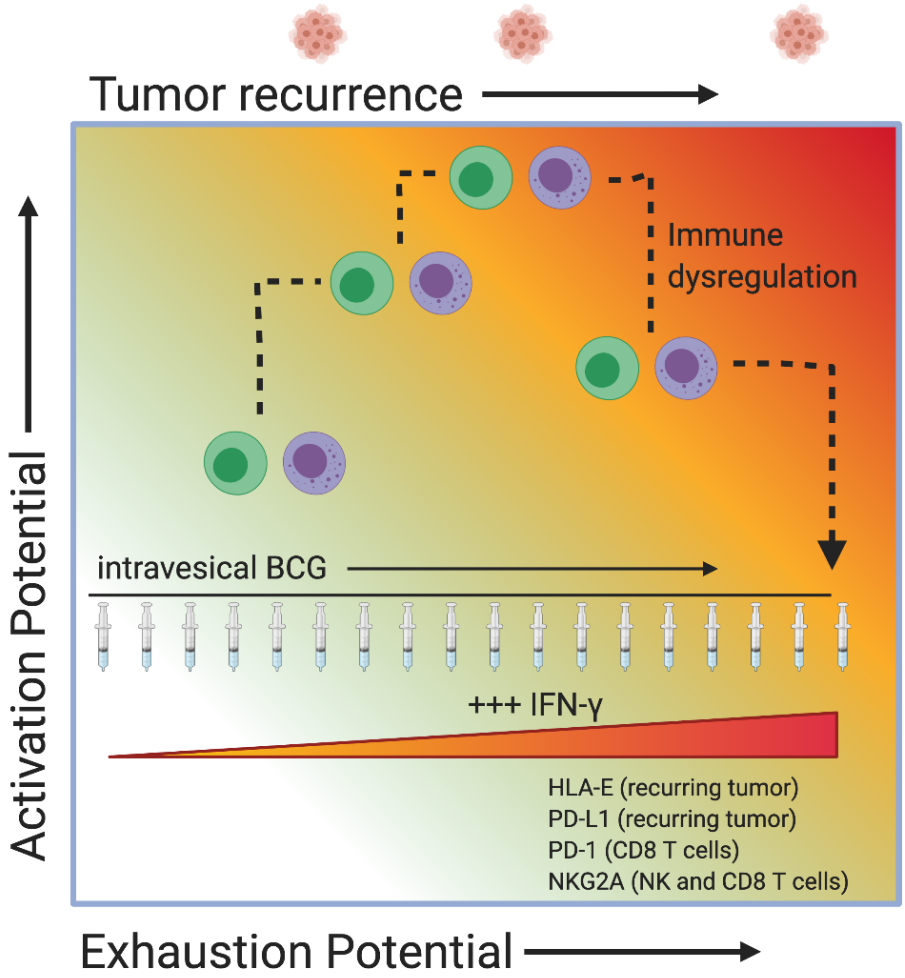

Figure 5: Schematic of proposed mechanism of immune dysregulation in the setting of chronic immune activation via BCG administration.

	Clinical Cohort Characteristics				
	HTG	OLINK Urine	Single Cell Seq	Spatial Seq	CYTOF
n samples, patients	36, 27	42, 26	6, 5	20, 9	16, 16
Female	4	2	0		1
BCG Naïve	19	26	2	4	0
BCG Unresponsive	17	-	4	5	16
Median Age	67.6	69.5	66.9		68.5
CIS	4	-			
Tis/Ta	5	-	1		8
T1	10	-	3		5
T2	0	-	0		2
T3	0	-	2		0
T4	0	-	0		1

Table 1: Clinical characteristics of experimental cohorts.

1. Redelman-Sidi G, Glickman MS, Bochner BH. The mechanism of action of BCG immunotherapy for bladder cancer--a current perspective. Nat Rev Urol **2014**;11(3):153-62 doi 10.1038/nrurol.2014.15.
2. Kamat AM, Li R, O'Donnell MA, Black PC, Roupret M, Catto JW*, et al.* Predicting Response to Intravesical Bacillus Calmette-Guerin Immunotherapy: Are We There Yet? A Systematic Review. Eur Urol **2018**;73(5):738-48 doi 10.1016/j.eururo.2017.10.003.
3. Müller G, Butea-Bocu M, Brock O, Hanske J, Pucheril D, Noldus J*, et al.* Association between Development of Metabolic Acidosis and Improvement of Urinary Continence after Ileal Neobladder Creation. J Urol **2020**;203(3):585-90 doi 10.1097/ju.0000000000000583.
4. Hedgepeth RC, Gilbert SM, He C, Lee CT, Wood DP, Jr. Body image and bladder cancer specific quality of life in patients with ileal conduit and neobladder urinary diversions. Urology **2010**;76(3):671-5 doi 10.1016/j.urology.2010.01.087.
5. Morales A. BCG: A throwback from the stone age of vaccines opened the path for bladder cancer immunotherapy. Can J Urol **2017**;24(3):8788-93.
6. Zlotta AR, van Vooren JP, Huygen K, Drowart A, Decock M, Pirson M*, et al.* What is the optimal regimen for BCG intravesical therapy? Are six weekly instillations necessary? Eur Urol **2000**;37(4):470-7 doi 10.1159/000020170.
7. Sfakianos JP, Salome B, Daza J, Farkas A, Bhardwaj N, Horowitz A. Bacillus Calmette-Guerin (BCG): Its fight against pathogens and cancer. Urol Oncol **2021**;39(2):121-9 doi 10.1016/j.urolonc.2020.09.031.
8. Sharma P, Hu-Lieskovan S, Wargo JA, Ribas A. Primary, Adaptive, and Acquired Resistance to Cancer Immunotherapy. Cell **2017**;168(4):707-23 doi 10.1016/j.cell.2017.01.017.
9. Gocher AM, Workman CJ, Vignali DAA. Interferon-γ: teammate or opponent in the tumour microenvironment? Nat Rev Immunol **2021** doi 10.1038/s41577-021-00566-3.
10. Benci JL, Johnson LR, Choa R, Xu Y, Qiu J, Zhou Z*, et al.* Opposing Functions of Interferon Coordinate Adaptive and Innate Immune Responses to Cancer Immune Checkpoint Blockade. Cell **2019**;178(4):933-48.e14 doi 10.1016/j.cell.2019.07.019.
11. Cheng L, Ma J, Li J, Li D, Li G, Li F*, et al.* Blocking type I interferon signaling enhances T cell recovery and reduces HIV-1 reservoirs. J Clin Invest **2017**;127(1):269-79 doi 10.1172/jci90745.
12. Teijaro JR, Ng C, Lee AM, Sullivan BM, Sheehan KC, Welch M*, et al.* Persistent LCMV infection is controlled by blockade of type I interferon signaling. Science **2013**;340(6129):207-11 doi 10.1126/science.1235214.
13. Wilson EB, Yamada DH, Elsaesser H, Herskovitz J, Deng J, Cheng G*, et al.* Blockade of chronic type I interferon signaling to control persistent LCMV infection. Science **2013**;340(6129):202-7 doi 10.1126/science.1235208.
14. Kates M, Matoso A, Choi W, Baras AS, Daniels MJ, Lombardo K*, et al.* Adaptive Immune Resistance to Intravesical BCG in Non-Muscle Invasive Bladder Cancer: Implications for Prospective BCG-Unresponsive Trials. Clin Cancer Res **2020**;26(4):882-91 doi 10.1158/1078-0432.Ccr-19-1920.
15. Rosenberg JE, Hoffman-Censits J, Powles T, van der Heijden MS, Balar AV, Necchi A*, et al.* Atezolizumab in patients with locally advanced and metastatic urothelial carcinoma who have progressed following treatment with platinum-based chemotherapy: a single-arm,

multicentre, phase 2 trial. Lancet **2016**;387(10031):1909-20 doi 10.1016/S0140-6736(16)00561-4.

16. Powles T, O'Donnell PH, Massard C, Arkenau HT, Friedlander TW, Hoimes CJ*, et al.* Efficacy and Safety of Durvalumab in Locally Advanced or Metastatic Urothelial Carcinoma: Updated Results From a Phase 1/2 Open-label Study. JAMA Oncol **2017**;3(9):e172411 doi 10.1001/jamaoncol.2017.2411.
17. Sharma P, Retz M, Siefker-Radtke A, Baron A, Necchi A, Bedke J*, et al.* Nivolumab in metastatic urothelial carcinoma after platinum therapy (CheckMate 275): a multicentre, single-arm, phase 2 trial. Lancet Oncol **2017**;18(3):312-22 doi 10.1016/S1470-2045(17)30065-7.
18. Patel MR, Ellerton J, Infante JR, Agrawal M, Gordon M, Aljumaily R*, et al.* Avelumab in metastatic urothelial carcinoma after platinum failure (JAVELIN Solid Tumor): pooled results from two expansion cohorts of an open-label, phase 1 trial. Lancet Oncol **2018**;19(1):51-64 doi 10.1016/S1470-2045(17)30900-2.
19. Grossman JE, Vasudevan D, Joyce CE, Hildago M. Is PD-L1 a consistent biomarker for anti-PD-1 therapy? The model of balstilimab in a virally-driven tumor. Oncogene **2021**;40(8):1393-5 doi 10.1038/s41388-020-01611-6.
20. Kamiya T, Seow SV, Wong D, Robinson M, Campana D. Blocking expression of inhibitory receptor NKG2A overcomes tumor resistance to NK cells. J Clin Invest **2019**;129(5):2094-106 doi 10.1172/jci123955.
21. Pereira BI, Devine OP, Vukmanovic-Stejic M, Chambers ES, Subramanian P, Patel N*, et al.* Senescent cells evade immune clearance via HLA-E-mediated NK and CD8(+) T cell inhibition. Nat Commun **2019**;10(1):2387 doi 10.1038/s41467-019-10335-5.
22. van Montfoort N, Borst L, Korrer MJ, Sluijter M, Marijt KA, Santegoets SJ*, et al.* NKG2A Blockade Potentiates CD8 T Cell Immunity Induced by Cancer Vaccines. Cell **2018**;175(7):1744-55.e15 doi 10.1016/j.cell.2018.10.028.
23. Seliger B, Jasinski-Bergner S, Quandt D, Stoehr C, Bukur J, Wach S*, et al.* HLA-E expression and its clinical relevance in human renal cell carcinoma. Oncotarget **2016**;7(41):67360-72 doi 10.18632/oncotarget.11744.
24. Liberzon A, Birger C, Thorvaldsdóttir H, Ghandi M, Mesirov JP, Tamayo P. The Molecular Signatures Database (MSigDB) hallmark gene set collection. Cell Syst **2015**;1(6):417-25 doi 10.1016/j.cels.2015.12.004.
25. Navratilova Z. Polymorphisms in CCL2&CCL5 chemokines/chemokine receptors genes and their association with diseases. Biomedical papers **2006**;150(2):191-204 doi 10.5507/bp.2006.028.
26. Maghazachi AA. Role of chemokines in the biology of natural killer cells. Curr Top Microbiol Immunol **2010**;341:37-58 doi 10.1007/82_2010_20.
27. Ito Y, Kikuchi E, Tanaka N, Kosaka T, Suzuki E, Mizuno R*, et al.* Down-regulation of NF kappa B activation is an effective therapeutic modality in acquired platinum-resistant bladder cancer. BMC Cancer **2015**;15:324 doi 10.1186/s12885-015-1315-9.
28. Monkley S, Overed-Sayer C, Parfrey H, Rassl D, Crowther D, Escudero-Ibarz L*, et al.* Sensitization of the UPR by loss of PPP1R15A promotes fibrosis and senescence in IPF. Sci Rep **2021**;11(1):21584 doi 10.1038/s41598-021-00769-7.

29. Jiang YH, Jhang JF, Hsu YH, Ho HC, Wu YH, Kuo HC. Urine cytokines as biomarkers for diagnosing interstitial cystitis/bladder pain syndrome and mapping its clinical characteristics. Am J Physiol Renal Physiol **2020**;318(6):F1391-f9 doi 10.1152/ajprenal.00051.2020.
30. Tyagi P, Barclay D, Zamora R, Yoshimura N, Peters K, Vodovotz Y*, et al.* Urine cytokines suggest an inflammatory response in the overactive bladder: a pilot study. Int Urol Nephrol **2010**;42(3):629-35 doi 10.1007/s11255-009-9647-5.
31. Browaeys R, Saelens W, Saeys Y. NicheNet: modeling intercellular communication by linking ligands to target genes. Nat Methods **2020**;17(2):159-62 doi 10.1038/s41592-019-0667-5.
32. Clancy-Thompson E, Perekslis TJ, Croteau W, Alexander MP, Chabanet TB, Turk MJ*, et al.* Melanoma Induces, and Adenosine Suppresses, CXCR3-Cognate Chemokine Production and T-cell Infiltration of Lungs Bearing Metastatic-like Disease. Cancer Immunol Res **2015**;3(8):956-67 doi 10.1158/2326-6066.CIR-15-0015.
33. Dengel LT, Norrod AG, Gregory BL, Clancy-Thompson E, Burdick MD, Strieter RM*, et al.* Interferons induce CXCR3-cognate chemokine production by human metastatic melanoma. J Immunother **2010**;33(9):965-74 doi 10.1097/CJI.0b013e3181fb045d.
34. Gresser I, Tovey MG, Maury C, Chouroulinkov I. Lethality of interferon preparations for newborn mice. Nature **1975**;258(5530):76-8 doi 10.1038/258076a0.
35. Madonna S, Scarponi C, Sestito R, Pallotta S, Cavani A, Albanesi C. The IFN-gamma-dependent suppressor of cytokine signaling 1 promoter activity is positively regulated by IFN regulatory factor-1 and Sp1 but repressed by growth factor independence-1b and Kruppel-like factor-4, and it is dysregulated in psoriatic keratinocytes. J Immunol **2010**;185(4):2467-81 doi 10.4049/jimmunol.1001426.
36. Liau NPD, Laktyushin A, Lucet IS, Murphy JM, Yao S, Whitlock E*, et al.* The molecular basis of JAK/STAT inhibition by SOCS1. Nat Commun **2018**;9(1):1558 doi 10.1038/s41467-018-04013-1.
37. Levine JH, Simonds EF, Bendall SC, Davis KL, Amir el AD, Tadmor MD*, et al.* Data-Driven Phenotypic Dissection of AML Reveals Progenitor-like Cells that Correlate with Prognosis. Cell **2015**;162(1):184-97 doi 10.1016/j.cell.2015.05.047.
38. Burkhardt DB, Stanley JS, 3rd, Tong A, Perdigoto AL, Gigante SA, Herold KC*, et al.* Quantifying the effect of experimental perturbations at single-cell resolution. Nat Biotechnol **2021**;39(5):619-29 doi 10.1038/s41587-020-00803-5.
39. Cristescu R, Mogg R, Ayers M, Albright A, Murphy E, Yearley J*, et al.* Pan-tumor genomic biomarkers for PD-1 checkpoint blockade-based immunotherapy. Science **2018**;362(6411) doi 10.1126/science.aar3593.
40. Wang L, Sfakianos JP, Beaumont KG, Akturk G, Horowitz A, Sebra RP*, et al.* Myeloid Cell-associated Resistance to PD-1/PD-L1 Blockade in Urothelial Cancer Revealed Through Bulk and Single-cell RNA Sequencing. Clin Cancer Res **2021** doi 10.1158/1078-0432.CCR-20-4574.
41. Spranger S, Spaapen RM, Zha Y, Williams J, Meng Y, Ha TT*, et al.* Up-regulation of PD-L1, IDO, and T(regs) in the melanoma tumor microenvironment is driven by CD8(+) T cells. Sci Transl Med **2013**;5(200):200ra116-200ra116 doi 10.1126/scitranslmed.3006504.

42. Rooney MS, Shukla SA, Wu CJ, Getz G, Hacohen N. Molecular and genetic properties of tumors associated with local immune cytolytic activity. Cell **2015**;160(1-2):48-61 doi 10.1016/j.cell.2014.12.033.
43. Ribas A. Adaptive Immune Resistance: How Cancer Protects from Immune Attack. Cancer Discov **2015**;5(9):915-9 doi 10.1158/2159-8290.Cd-15-0563.
44. Grasso CS, Tsoi J, Onyshchenko M, Abril-Rodriguez G, Ross-Macdonald P, Wind-Rotolo M*, et al.* Conserved Interferon-γ Signaling Drives Clinical Response to Immune Checkpoint Blockade Therapy in Melanoma. Cancer Cell **2020**;38(4):500-15.e3 doi 10.1016/j.ccell.2020.08.005.
45. Gocher AM, Workman CJ, Vignali DAA. Interferon-γ: teammate or opponent in the tumour microenvironment? Nat Rev Immunol **2022**;22(3):158-72 doi 10.1038/s41577-021-00566-3.
46. Chang SS, Boorjian SA, Chou R, Clark PE, Daneshmand S, Konety BR*, et al.* Diagnosis and Treatment of Non-Muscle Invasive Bladder Cancer: AUA/SUO Guideline. J Urol **2016**;196(4):1021-9 doi 10.1016/j.juro.2016.06.049.
47. Marshall A, Celentano A, Cirillo N, McCullough M, Porter S. Tissue-specific regulation of CXCL9/10/11 chemokines in keratinocytes: Implications for oral inflammatory disease. PLoS One **2017**;12(3):e0172821 doi 10.1371/journal.pone.0172821.
48. A. Martinez-Marti MM, F. Barlesi, E. Carcereny Costa, Q. Chu, I. Monnet, A. Sanchez, S. Dahkil, D..R. Camidge, P. He, Y. Soo-Hoo10, Z. Cooper, R. Kumar, J. Bothos, C. Aggarwal, R.S. Herbst. COAST: An open-label, randomised, phase II platform study of durvalumab alone or in combination with novel agents in patients with locally advanced, unresectable, stage III NSCLC. Annals of Oncology **2021**;32 doi 10.1016/annonc/annonc741.
49. Shapiro SS, Wilk MB. An Analysis of Variance Test for Normality (Complete Samples). Biometrika **1965**;52(3/4):591-611 doi 10.2307/2333709.
50. Kruskal WH, Wallis WA. Use of Ranks in One-Criterion Variance Analysis. Journal of the American Statistical Association **1952**;47(260):583-621 doi 10.2307/2280779.
51. Hao Y, Hao S, Andersen-Nissen E, Mauck WM, 3rd, Zheng S, Butler A*, et al.* Integrated analysis of multimodal single-cell data. Cell **2021**;184(13):3573-87.e29 doi 10.1016/j.cell.2021.04.048.
52. Zhang X, Lan Y, Xu J, Quan F, Zhao E, Deng C*, et al.* CellMarker: a manually curated resource of cell markers in human and mouse. Nucleic Acids Res **2019**;47(D1):D721-d8 doi 10.1093/nar/gky900.
53. Glass DR, Tsai AG, Oliveria JP, Hartmann FJ, Kimmey SC, Calderon AA*, et al.* An Integrated Multi-omic Single-Cell Atlas of Human B Cell Identity. Immunity **2020**;53(1):217-32.e5 doi 10.1016/j.immuni.2020.06.013.
54. Magri G, Comerma L, Pybus M, Sintes J, Lligé D, Segura-Garzón D*, et al.* Human Secretory IgM Emerges from Plasma Cells Clonally Related to Gut Memory B Cells and Targets Highly Diverse Commensals. Immunity **2017**;47(1):118-34.e8 doi 10.1016/j.immuni.2017.06.013.
55. Rouillard AD, Gundersen GW, Fernandez NF, Wang Z, Monteiro CD, McDermott MG*, et al.* The harmonizome: a collection of processed datasets gathered to serve and mine knowledge about genes and proteins. Database (Oxford) **2016**;2016 doi 10.1093/database/baw100.

56. Galon J, Robertson MW, Galinha A, Mazières N, Spagnoli R, Fridman WH*, et al.* Affinity of the interaction between Fc gamma receptor type III (Fc gammaRIII) and monomeric human IgG subclasses. Role of Fc gammaRIII glycosylation. Eur J Immunol **1997**;27(8):1928-32 doi 10.1002/eji.1830270816.
57. Liberzon A, Subramanian A, Pinchback R, Thorvaldsdóttir H, Tamayo P, Mesirov JP. Molecular signatures database (MSigDB) 3.0. Bioinformatics **2011**;27(12):1739-40 doi 10.1093/bioinformatics/btr260.

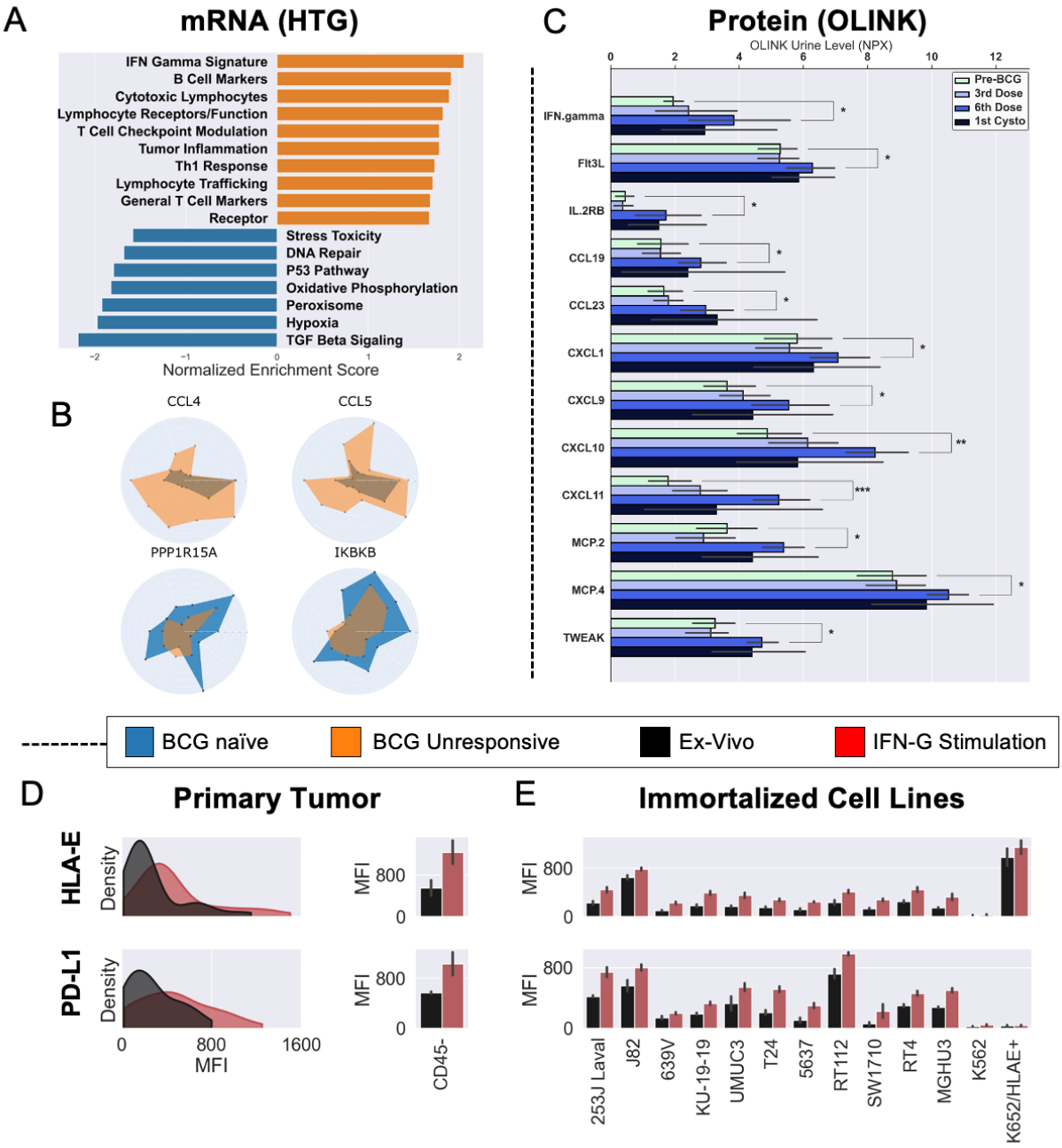

Figure 1: Adaptive resistance in BCG unresponsive disease revealed by bulk RNA sequencing and OLINK proteomics. **A:** Bulk RNA gene-set enrichment analysis showing statistically significant differences between BCG naïve and BCG unresponsive cases. IFN-γ signature is the most highly upregulated signature in the BCG unresponsive patients. All gene sets are significant at $p < 0.05$ by Kruskal-Wallis or independent T-test. **B:** Radar plots, one patient per spoke, showing upregulated individual genes (CCL4 and CCL5), and downregulated individual genes (PPP1R15A and IKBKB). All genes significant at $p < 0.05$. **C:** Longitudinal protein analysis in all patients with comparisons between BCG naïve and 6th induction dose timepoints (* $p < 0.05$, ** $p < 0.001$, *** $p < 0.0001$). **D:** MFI of primary non-muscle invasive bladder cancer cells after 24 hours of incubation with IFN-γ. **E:** MFI of commercial immortalized cell lines after 24 hours of IFN-γ stimulation (all values $p < 0.05$).

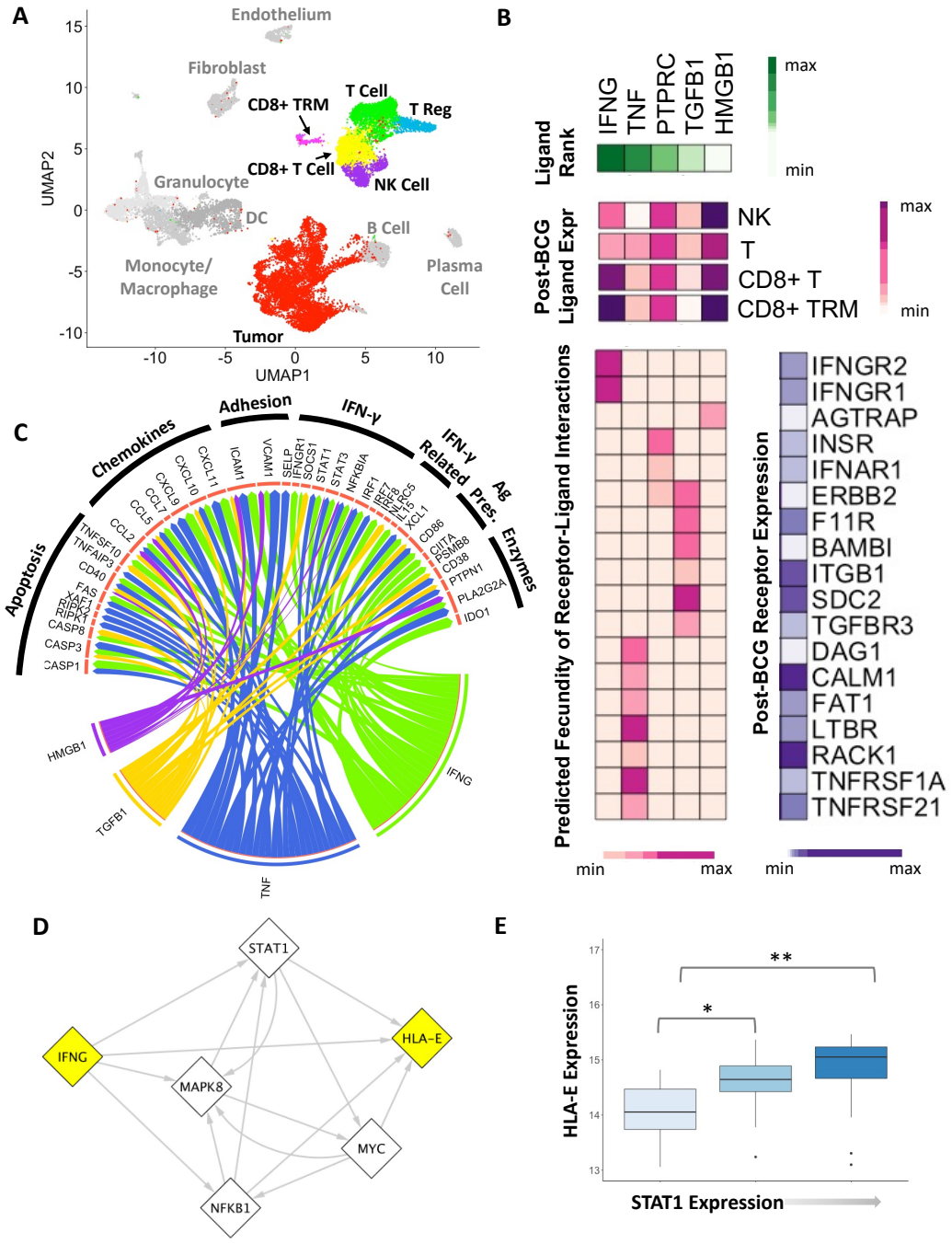

Figure 2: IFN-γ signaling is predicted to drive downstream HLA-E expression via STAT1 in tumor cells. **A:** UMAP visualization of cell types from scRNA-Seq analysis of urothelial tumor samples. **B:** NicheNet predictions of upstream ligand-receptor interactions showing IFNG, TNF, PTPRC, TGFB1, and HMGB1 (left) as the top 5 ligands expressed in NK, T, CD8+ T, and CD8+ TRM cells (middle) that most likely influence tumor cell expression of interferon-gamma signaling genes. Strength of ligand-receptor interactions (top right) and expression of the receptors in tumor cells (bottom right) are also shown. **C:** Circos plot showing links between NicheNet-predicted ligands and downstream interferon-gamma pathway genes. Strong relationships between ligand-target gene pairs are demonstrated by both wider arrow width and solid arrow colors. **D:** NichetNet-predicted regulatory network between IFN-γ and HLA-E. **E:** Expression of HLA-E in HTG targeted RNA-Seq urothelial cancer cohort with respect to STAT1 levels. (*p = 0.0274; **p = 0.00674)

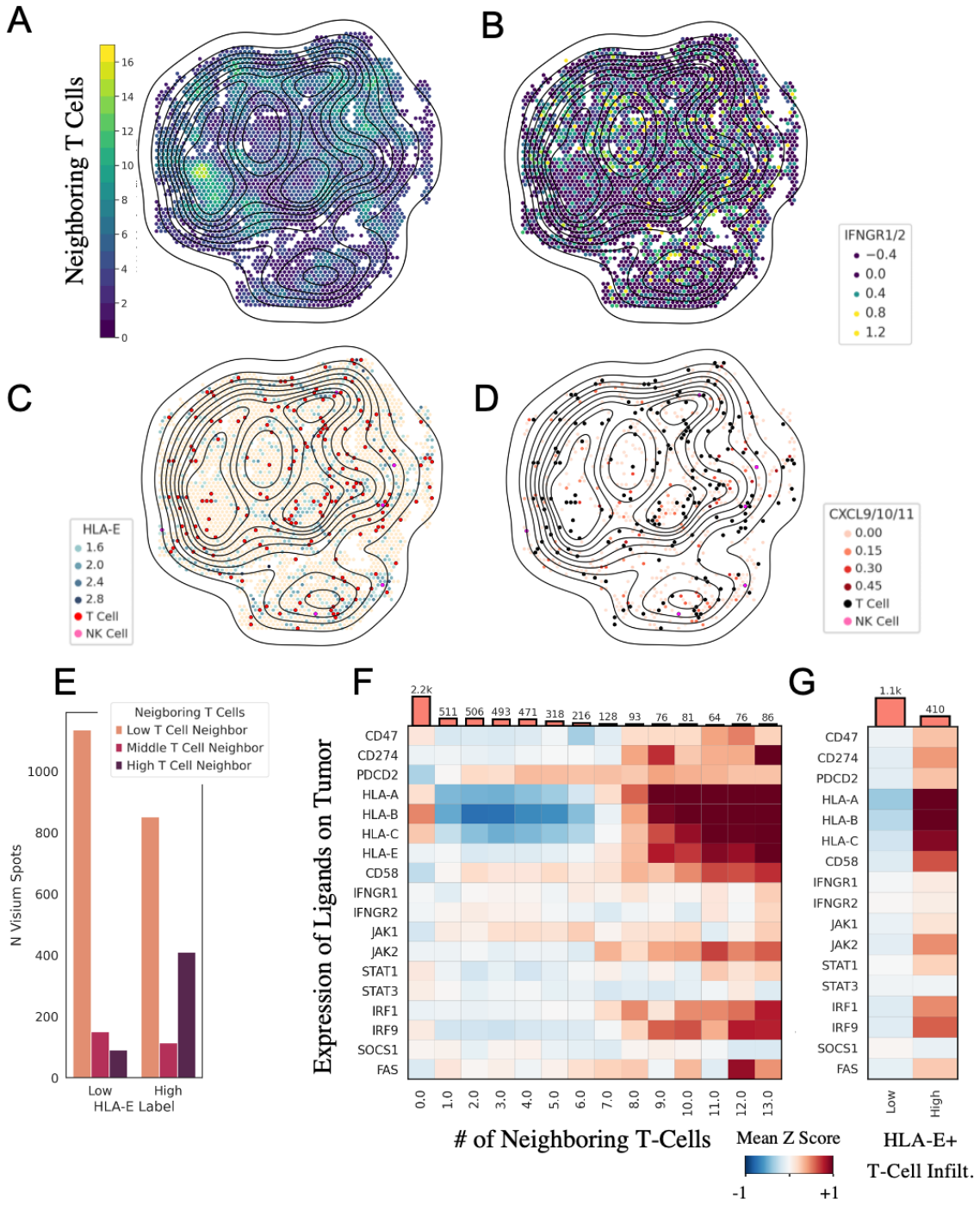

Figure 3: Preferential tumor "nano-environment" infiltration of T cells occurs in tumor nests with higher densities of HLA-E. **A:** representative spatial slice colored by number of neighboring infiltrating T cells, with a topographical plot showing density of HLA-E expression. **B:** representative spatial slice colored by *IFNGR1* and *IFNGR2* score with a topographical plot overlaid showing density of HLA-E expression. **C:** representative spatial slice colored by low HLA-E expressing cells (tan), high HLA-E expressing cells (blue) and immune cells (red and magenta), with a topographical plot overlaid showing density of HLA-E expression. **D:** representative spatial slice showing CXCL9/10/11 score, T cells, NK cells, and an overlaid topographical plot of HLA-E density. **E:** Barplot showing counts of low and high HLA-E tumor cells by surrounding T cell classification (low, medium, and high infiltration).
F: heatmap of all spatial points, BCG naïve and unresponsive, showing pertinent genes z-scored and stratified by number of neighboring infiltrating T-cells. **G:** heatmap of low-HLA-E and low-T cell infiltrated tumor cells vs high-HLA-E and high-T cell infiltrated tumors.

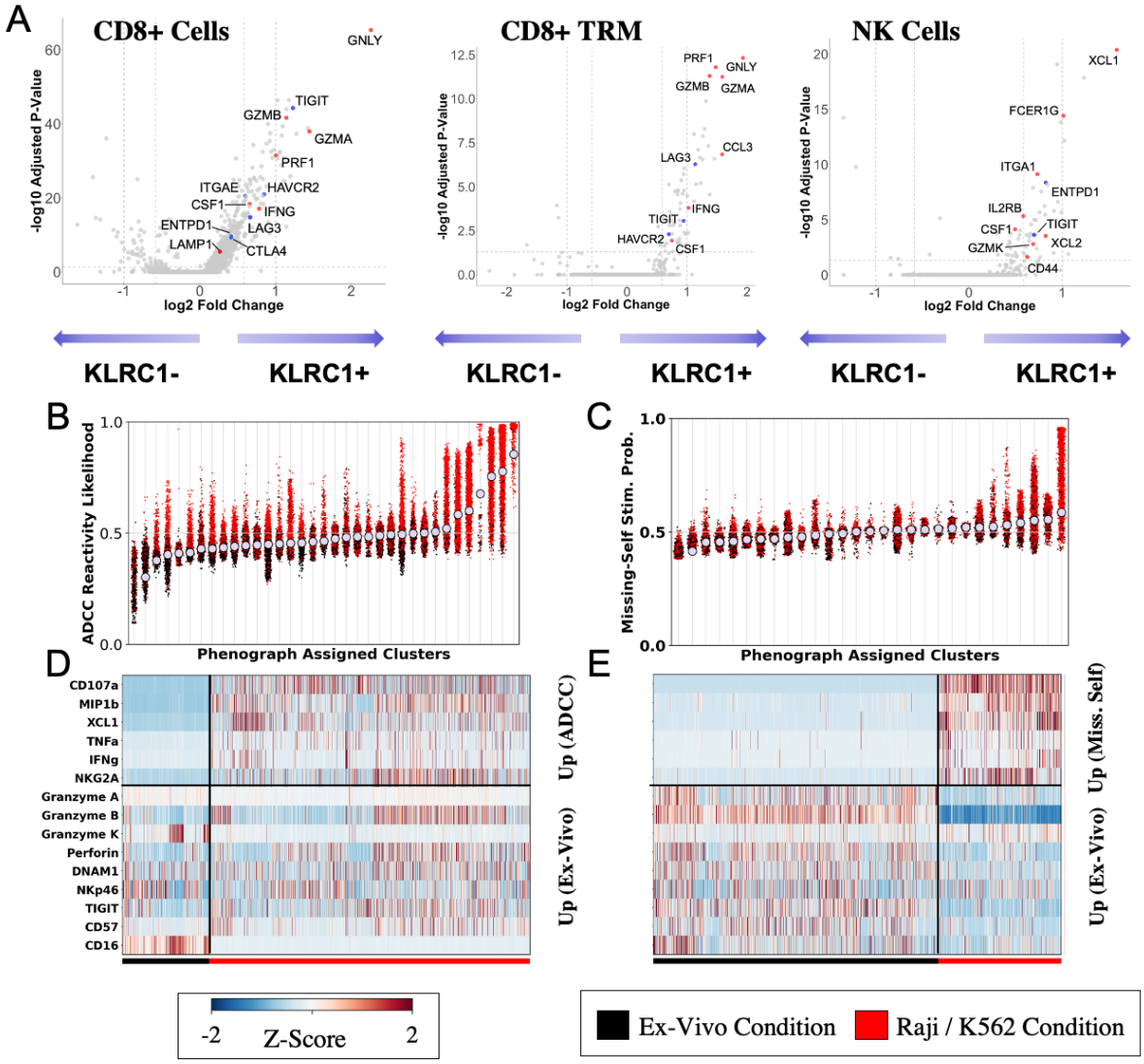

Figure 4: *KLRC1* (NKG2A) expression stratifies NK and CD8+ T cell capacity for anti-tumor functions in BCG unresponsive tumors. A: single-cell RNA sequencing showing statistically significant upregulation of both immune checkpoints and cytotoxic genes in KLRC1+ CD8+ T cells, CD8+ TRMs, and NK cells. B: phenograph clusters stratified by ADCC reactivity. C: phenograph clusters stratified by missing-self reactivity. D: CYTOF markers partitioned by strongly ex-vivo vs strongly ADCC reactive clusters. E: CYTOF markers partitioned by strongly ex-vivo and strongly missing-self reactive clusters.

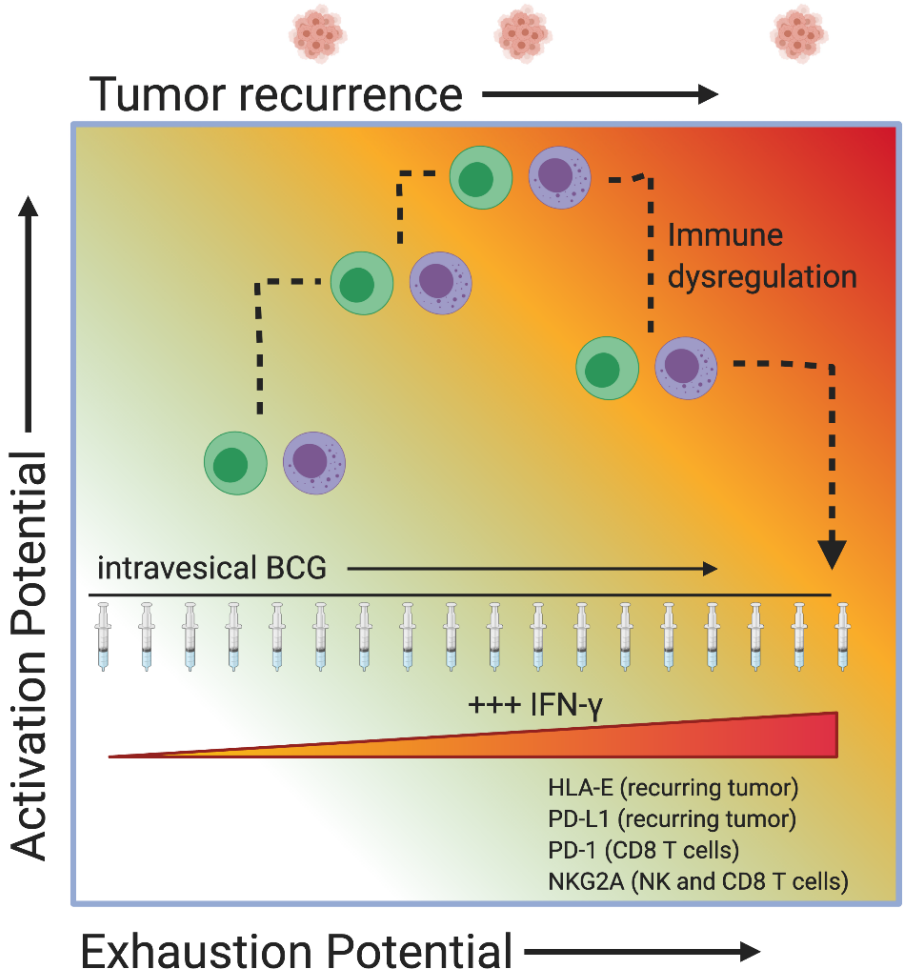

Figure 5: Schematic of proposed mechanism of immune dysregulation in the setting of chronic immune activation via BCG administration.

	Clinical Cohort Characteristics				
	HTG	OLINK Urine	Single Cell Seq	Spatial Seq	CYTOF
n samples, patients	36, 27	42, 26	6, 5	20, 9	16, 16
Female	4	2	0		1
BCG Naïve	19	26	2	4	0
BCG Unresponsive	17	-	4	5	16
Median Age	67.6	69.5	66.9		68.5
CIS	4	-			
Tis/Ta	5	-	1		8
T1	10	-	3		5
T2	0	-	0		2
T3	0	-	2		0
T4	0	-	0		1

Table 1: Clinical characteristics of experimental cohorts.